DISSERTATION

Ionization Dynamics of Atoms in Femto- and Attosecond Pulses

ausgeführt zum Zwecke der Erlangung des akademischen Grades eines
Doktors der Technischen Wissenschaften
unter der Leitung von

O.Univ.Prof. Joachim Burgdörfer
Institut für Theoretische Physik, TU-Wien
und
Univ. Distinguished Prof. Chii-Dong Lin
Physics Department, Kansas State University, USA

eingereicht an der Technischen Universität Wien
Fakultät für Physik
von

Dipl.-Ing. Marlene Wickenhauser
Matr.-Nr. 9725916
Löhrgasse 19/28, A-1150-Wien

Wien, am 6 Juni 2006

Acknowledgment

I want to start my thesis with expressing my thanks to those people who have supported and motivated me during my time as a PhD student. My two advisors, Joachim Burgdörfer and Chii-Dong Lin have both done a terrific job in guiding me through my studies. In the first two year of my thesis, in Vienna, I was able to work quite independently on my topic of time-resolved Fano resonances. I am especially indebted to Joachim Burgdörfer for motivating me to work on this topic. Furthermore, I want to thank Joachim for making it possible for me to spend the last years of my PhD in the USA. While studying the details of a Fano resonance, I learned as well a lot about femto- and attosecond laser pulses. At this point I want to acknowledge the work of F. Krausz and his group who made Vienna one of the frontier research places of attosecond physics. In particular I want to thank Mathias Uiberacker and Reinhard Kienberger who gave me a tour of the laser laboratory and during many helpful discussions explained to me the experimental side of my PhD topic. Furthermore, I was very glad when I by chance found out that the group of Armin Scrinzi from the photonics institute was working on a topic related to my studies. I am indebted to Armin Scrinzi, Olga Smirnova and Vladislav Iakovlev for detailed discussions which helped me a lot. Especially, I want to thank Olga Smirnova for introducing the Russian laser community to me during a workshop in Hamburg. Christoph Lemell, Florian Libisch and Beate Solleder have been great office mates during my stay in Vienna, where I am especially grateful to Christoph for all his help and technical support in computing. Furthermore, I enjoyed physics discussions with Imre Barna and Emil Persson. The later not only explained to me numerical concepts of laser-atom interaction, but as well had a detailed knowledge on avoided crossings which finally led to the invitation of his thesis advisor, Ingrid Rotter. I want to thank Ingrid Rotter for her interest in my work and for many helpful and encouraging discussions about Fano resonances in a laser field. Furthermore, I want to thank Karoly Tokesi for pleasant conversations during his visits to Vienna and for the cactus he gave to me. Last but not least from my Vienna colleagues I want to thank Severin Puschkarski who could convince me that atomic physics is a far more interesting subject than high-energy physics while drinking tea together during working on our master degree.

I am very much indebted to Chii-Dong Lin, his group and many other

members of Kansas State University who have supported and helped me during my stay at KSU from the very beginning. I gratefully appreciate that my advisor, Chii-Dong Lin, accepted to host me for a year in his group. I want to thank Chii-Dong for spending so much time on discussing physics with me and all the good advice he gave me during my stay in his group. He not only taught me how to lead my research project, how to write papers and present my results in a talk, but also made sure that I do my homework for class and participate in the final exam. I owe a lot to Xiao-Min Tong, with whom I had the pleasure to collaborate at KSU and who taught me many technical details about solving the time-dependent Schrödinger equation. Furthermore, I want to thank Zengxiu Zhao and Anh-Thu Le for all their help and support in physics and aspects of daily life in the USA. From all those with whom I enjoyed interesting and helpful physics discussions I want to mention especially: Thomas Niederhausen, for working on CD Lin's homework problems together with me, so that together we finally never needed more than four hours for solving a certain problem. Uwe Thumm, for asking me to join lunch with his group. Fatima Anis, Remigio Trujillo, Vladimir Roudnev and Jose D'Incao for being good colleagues at KSU. Ali Alnaser, Chakra Maharjan and Predrag Ranitovic for being patient enough to explain their COLTRIMS experiments to a theorist. Furthermore, I want to thank Thomas and his French House crew for organizing the best parties of Manhattan.

The last item in this long list of acknowledgments is reserved for my family for their help and support during my studies.

Deutsche Kurzfassung

Eine der grundlegensten physikalischen Untersuchungsmethoden ist die Spektroskopie. Hochauflösende Laserspektroskopie ermöglicht heutzutage Präzissionsstudien an feinsten Details der Spektren. Eine ganz andere Art der Spektroskopie ist hingegen erst vor wenigen Jahren durch die experimentelle Realisierung einzelner Femto- und Attosekunden Laserpulse möglich geworden. Diese Pulse erlaubten erstmals die direkte Beobachtung von Molekülbewegungen und der Bewegung von Elektronen in Atomen. Die rasante Entwicklung in den letzten Jahren im Bereich der experimentellen Laserphysik brachte auch neue Herausforderungen für die Theorie. Es stellte sich heraus, dass schon in scheinbar einfachen atomaren Systemen mit wenigen Freiheitsgraden, wie zum Beispiel in dem von uns untersuchten Fall einer Fano Resonanz, interessante und vielschichtige Effekte auftreten können, deren theoretische Beschreibung alles andere als einfach ist.

In dieser Dissertation wird zuerst am Beispiel der Ionization von Argon mit Femtosekunden Laserpulsen von hoher Intensität die ab-initio Lösung der zeitabhängigen Schrödinger Gleichung mit einer approximativen Lösung verglichen. Das Näherungsmodell beruht auf der häufig verwendeten Methode der 'Strong Field Approximation (SFA)', welche den Ionizationsprozess anschaulich and qualitativ erfolgreich beschreibt. Wir erzielten eine unerwartet gute Übereinstimmung beider Rechnungen, aus welcher interessante physikalische Konsequenzen über die Relevanz des Coulomb Potentials während der Ionization folgen. Unsere Rechnungen sind auch in guter Übereinstimmung mit einem kürzlich durchgeführtem Experiment. Weiters untersuchten wir die zeitliche Entwicklung einer Fano Resonanz welche mit einem attosekunden Puls angeregt wurde. Während die zeitintegralen Eigenschaften einer Fano Resonanz spätestens seit den sechziger Jahren im Detail verstanden sind berechneten wir zum ersten Mal die zeitabhängige Ionizationswahrscheinlichkeit für eine solche Resonanz. Um Informationen über den Zerfallsprozess zu erhalten, wird neben dem anregenden attosekunden Puls ein zweiter Abfrage Laser verwendet. Die im ersten Teil der Dissertation bewiesene, gute Übereinstimmung der SFA mit der ab-initio Rechnung, erlaubte es uns, die Fano Resonanz im Feld des Lasers, was ein Mehr-Elektronen Problem mit starker Korrelation der beteiligten Elektronen darstellt, mit Hilfe der SFA zu berechnen. Experimente in diese Richtung sind geplant.

Abstract

One of the most fundamental experimental techniques in physics is spectroscopy. High-precision measurements of atomic transition energies in atomic systems provide today detailed information about the atomic-structure. However, a new way of doing spectroscopy became possible with the recent production of isolated femto- and attosecond laser pulses. With these pulses chemical reactions and the 'movement' of electrons inside atoms can be studied directly in the time domain. It became obvious, that even simple atomic systems with only a few degrees of freedom, as for example the case of a Fano resonance in the field of a short pulse, suddenly show an interesting and complex behavior.

In the first chapters of this thesis we compare an ab-initio solution of the time-dependent Schrödinger equation with an approximative solution, for the case of ionization of argon with intense, short laser pulses. The approximative method is based on the strong-field approximation (SFA) which is one of the most popular methods in this field. In the SFA model the influence of the core potential on the ionized electrons is neglected and all bound states except the ground state are neglected as well. Nevertheless, we obtained a surprisingly good agreement between the two calculations, which lead to interesting consequences concerning the relevance of the Coulomb potential in the ionization process. Our calculations are in good agreement with a recently performed experiment. Furthermore, we have studied the temporal evolution of a Fano resonance excited by an attosecond laser pulse. While the time-integral properties of a Fano resonance are well known since the sixties, we have been among the first to calculate the time-dependent ionization probability of such a resonance. To gain information about the time evolution of the decaying resonance, a second probe laser pulse has to be applied in addition to the attosecond pulse. Since in the first part of this thesis we could show the reliability of the SFA model, we applied this approximation to calculate the Fano resonance in the external laser field. Experiments in this direction are planned.

Contents

List of Figures

Chapter 1

Introduction

Recent progress in ultrafast optics has allowed the generation of intense light pulses of only a few cycles duration (Steinmeyer et al. [1], Baltuska et al. [2], Nisoli et al. [3], Morgner et al. [4], Sutter et al. [5], Shirakawa et al. [6]). Due to this extreme temporal confinement of light, moderate pulse energies of the order of one microjoule can result in peak intensities higher than 10^{15} W/cm^2 (Brabec and Krausz [7]). These field strengths exceed that of the Coulomb field experienced by outer-shell electrons in atoms. As a consequence the laser field is strong enough to suppress the binding Coulomb potential and to trigger optical field ionization in a highly nonlinear process (Keldysh [8]). In contrast to longer laser pulses comprising of many field oscillations, in a few-cycle pulse high intensities can be switched on within a few optical periods lasting merely a few femtoseconds. Thus, detachment of the first electron is completed at substantially higher field strengths and a substantial fraction of the atoms is ionized during one laser oscillation period. The sine-like variation of the laser field produces pronounced peaks in the ionization signal at times near maximum field strength. The resulting short electron wave packets can be accelerated by the laser field and directed back to the parent ion. Rescattering with the parent ion after roughly one half-cycle of the laser field creates a broadband radiation with energies that are proportional to the frequency of the laser field. By applying a spectral filter and compensating chirp one can generate single bursts of XUV radiation with durations as short as 250 as (Hentschel et al. [9]).

With the availability of such pulses previously inaccessible regimes of

nonlinear optics are now being entered. Rather than accumulating an effect over many optical periods, as in conventional optics, the electric field can take direct control of the electronic motion and imprint its time structure on electron momentum and position. The direct observation of the motion of electrons inside atoms occurring on an attosecond time scale becomes now feasible.

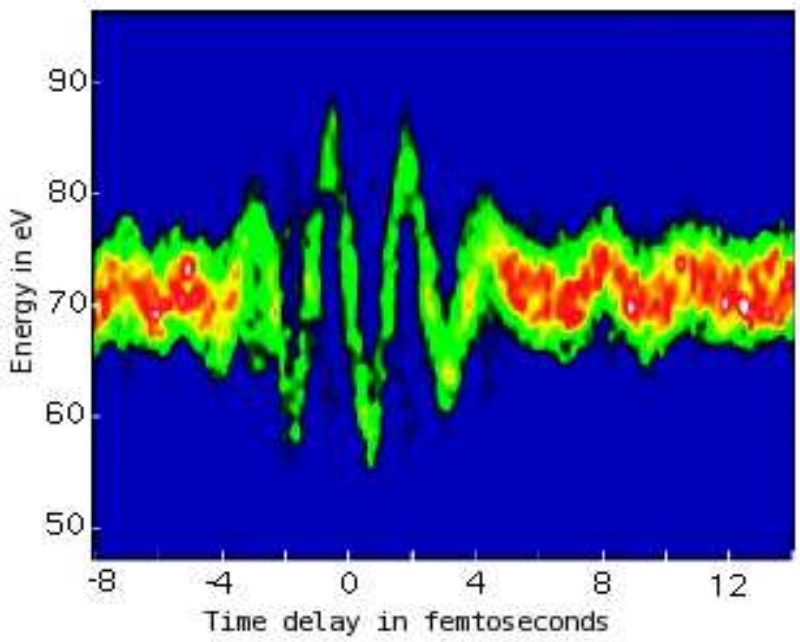

Figure 1.1: Figure taken from E. Goulielmakis et al., SCIENCE **305** (2004). Experimental results for a series of kinetic energy spectra of electrons detached from neon atoms in the presence of an intense < 5 fs laser field with a wavelength of 750 nm in false-color representation. The delay of the attosecond probe pulse was varied in steps of 200 as. The detected electrons were ejected along the direction of the laser polarization with a mean initial kinetic energy of 71.5 eV.

Fig. 1.1 taken from E. Goulielmakis et al., SCIENCE **305** (2004) (Goulielmakis et al. [10]), shows experimental spectra obtained in a photoionization process, where the ionizing pulse lasts only 250 as. A second, optical laser pulse is present during the ionization process. A series of spectra with vary-

ing time-delay between the attosecond and the optical pulse are shown in Fig. 1.1. The energy shift of the electrons versus the timing of the attosecond pulse directly presents the vector potential $A(t)$ of the optical laser field. Thus the generation of single attosecond pulses together with a well synchronized optical laser pulse made it possible to directly probe the light field oscillations in a few-cycle pulse. This same technique can also be applied to study electronic motion deep inside atoms in the time-domain, as has been done in a proof-of principle experiment for an Auger decay in Krypton (Drescher et al. [11], Smirnova et al. [12]). However, the future evolution of time-resolved atomic physics critically depends on the progress in theory and the understanding of the dynamics of strong-fields and attosecond pulses interacting with atomic targets.

We therefore investigate in this thesis the detailed ionization dynamics of atoms subject to femto- and attosecond pulses. In the first chapters we present results of a comparison between an ab-initio solution of the time-dependent Schrödinger equation (TDSE) and an approximate solution based on the strong-field approximation (SFA) (Lewenstein et al. [13], Wickenhauser et al. [14, 15]). Because of its simplicity, both in the numerical implementation as well as in the physical interpretation, the SFA approximation is one of the most popular models used in this field. The time-dependent Schrödinger equation is solved with a generalized pseudospectral method in the energy representation (Tong and Chu [16, 17]). We compare the energy spectra as well as the angle-resolved momentum distributions obtained with the SFA and the TDSE calculation for the case of above-threshold ionization (ATI) of a rare gas with an optical laser pulse. Since it has been shown that the process of above-threshold ionization in a laser pulse with intensity of about 10^{14} W/cm^2 can be successfully described within an effective one-electron model (Wiehle et al. [18]) this process is a good testing case for the applicability of the SFA model.

In contrast to a longer laser pulse, the intensity and frequency of a few-cycle pulse are not well defined. In chapter three we discuss the subpeaks in the spectra caused by the changing intensity in the short pulse (Wickenhauser et al. [14], Bardsley et al. [19]). Since the energy positions of the levels shift in the laser field, the effective ionization potential an electron

experiences in the ionization process depends on the intensity at the time of ionization. Thus, electrons ionized during different cycles of the laser field do not add up coherently which causes the ATI peaks to split up into several subpeaks. We show that positions of these peaks shift with the intensity, where we see that within one ATI peak this shift is not constant. In the angle-resolved momentum spectra these subpeaks have the same parity within one ATI peak. The detailed analysis of the angle-resolved momentum spectra is presented in chapter four. We found a surprisingly good agreement between the SFA and the full numerical TDSE calculation. Despite the fact that the SFA calculation severely underestimates the total ionization probability, it obviously still contains detailed information about the 2D momentum distributions. We show that all ATI peaks with their corresponding subpeaks can be understood with the simple SFA model. Also the parity and the dominant angular momentum can be reproduced in most cases within the SFA approximation. However, since the SFA model neglects the intermediate resonances in the ionization process and the effect of the Coulomb potential on the ionized electrons, it is impossible to predict the momentum distribution exactly. We present a detailed discussion of the limitations of the SFA model. In addition, all our calculations are relevant for recent experiments (Rudenko et al. [20], Maharjan et al. [21]).

Starting with chapter five we discuss the ionization dynamics of an attosecond pulse exciting a Fano resonance. While the time-integral features of a Fano resonance are well understood since the sixties, we study the time dependent aspects of an autoionizing decay (Fano [22, 23], Lambropoulos and Zoller [24], Wickenhauser et al. [25], Zhao and Lin [26]). This study is motivated by the recent availability of single attosecond pulses. While it is already well known (Jones [27], Reinhold et al. [28], Ahn et al. [29]) that with nano-and picosecond pulses the wave packet dynamics of Rydberg atoms can be resolved in the time domain, attosecond pulses now allow the time-resolved study of inner-shell processes occurring on an atto- and femtosecond time scale. In a first experiment (Drescher et al. [11]) the lifetime of an Auger decay lasting 8 fs was measured using a pump-probe technique. In this experiment the attosecond pulse excites the resonant state and a second probe laser is applied with a well controlled delay time between pump and probe pulse. A series of energy spectra are recorded for different pump-probe

delays. From these spectra the lifetime of the Auger decay can be finally extracted (Smirnova et al. [12]). We simulated in this thesis such a pump-probe experiment for the case of the excitation of a Fano resonance. In contrast to the Auger decay, in which only one ionization channel is involved, the typical asymmetric Fano line shape is caused by the interference of two ionization channels. An electron is either directly ionized or it is emitted during the decay of the resonant state. From the spectral line shape of a Fano resonance it is possible to obtain information about the lifetime of the resonant state and the relative ratio of the population of the two channels. However, we can show that due to the different time scales involved in the two channels, a fast direct ionization and a delayed resonant ionization, these two ionization channels can be distinguished in the pump-probe spectra. All simulations of the pump-probe experiment have been performed within the SFA approximation, justified by the detailed study of chapters three and four.
In the last chapter we have generalized our study to the excitation of two (overlapping) resonances (Zhao and Lin [26], Wickenhauser et al. [30]). We find that in this case a beating signal can be found in the energy spectra of ionized electrons, where the beating frequency is proportional to the energy spacing between the two resonances. We show that this signal is almost identical to the time-differential ionization probability which proves that non-trivial information about the ionization process happening on a femtosecond time scale can be directly extracted from the pump-probe spectra.

Chapter 2

Theoretical Methods for Single-Electron Systems

In this chapter the basic theoretical concepts of laser-atom interaction relevant for this thesis will be presented. The interaction of an atom with an external electromagnetic field is most easily described by treating the field classically and inserting the corresponding potentials as functions in the Hamiltonian. This procedure, however, cannot account for the observed phenomenon of spontaneous emission, in which an excited atom emits a photon in the absence of an external field. For a consistent description of the electromagnetic transition including this effect, the field must be treated quantum mechanically. However, in this thesis we use a classical description of the electromagnetic field.
The scalar potential $\Phi(\mathbf{r},t)$ and the vector potential $\mathbf{A}(\mathbf{r},t)$ together define the electric field $\mathbf{E}(\mathbf{r},t)$ and the magnetic field $\mathbf{B}(\mathbf{r},t)$. For the intensities relevant here ($I < 10^{15}$ W/cm^2) the magnetic field can be neglected (Friedrich [31], Diels and Rudolph [32]).

2.1 Hamiltonian

The Hamiltonian for an atom with a single active electron interacting with a laser field is then

$$H = \frac{(\mathbf{p} + \frac{1}{c}\mathbf{A}(\mathbf{r},t))^2}{2} + \Phi(\mathbf{r},t) + V(\mathbf{r}), \tag{2.1}$$

where c is the speed of light and $V(\mathbf{r})$ is the effective atomic potential.
For most purposes, the interaction with the field can be described in the dipole approximation, i.e. one can neglect spatial variations of the field. This approximation is valid because the spatial extension of the interacting system, in this case an atom, is in general much smaller than the wavelength of the laser. Typically, femtosecond laser pulses are generated with a Ti:sapphire laser with a carrier wavelength of about 800 nm. The shortest wavelength considered in this thesis corresponds to an attosecond pulse with a wavelength of 12.4 nm. However, compared to the Bohr radius of 0.05 nm this is still large. Thus, in dipole approximation the field $\mathbf{E}(\mathbf{r}, t)$ can be written as $\mathbf{E}(t)$.

2.2 Gauge Freedom

The electric field remains unchanged when the potentials Φ and $\mathbf{A}$ are replaced by new potentials Φ' and $\mathbf{A}'$ which are related to the original potentials by the following transformation (Jackson [33]):

$$\begin{aligned} \mathbf{A}' &= \mathbf{A} + \nabla\Lambda, \\ \Phi' &= \Phi - \frac{1}{c}\frac{\partial\Lambda}{\partial t} \end{aligned} \tag{2.2}$$

Since the Hamiltonian (2.1) contains the potentials $\mathbf{A}$ and Φ and not the physical fields, it depends on the particular choice of gauge. Observable quantities, such as energy differences and transition probabilities are, however, independent of this choice. The most commonly used gauges for laser-atom interaction calculations are the length- and the velocity gauge. The Hamiltonian in length gauge is:

$$H = \frac{\mathbf{p}^2}{2} + \mathbf{r}\mathbf{E}(t) + V(\mathbf{r}). \tag{2.3}$$

The velocity gauge form is familiar as the minimal coupling from field theory. The scalar field is zero in this gauge and the Hamiltonian takes on the form:

$$H = \frac{(\mathbf{p} + \frac{1}{c}\mathbf{A}(t))^2}{2} + V(\mathbf{r}). \tag{2.4}$$

Although equivalent up to a unitary transformation, the two gauges behave differently when approximations are made.

An important consequence of external fields is that the Hamiltonian is in general no longer rotationally invariant. However, for spatially homogeneous fields the Hamiltonian does remain invariant under rotations around the polarization axis, so that the component of the total angular momentum in the field direction remains a constant of motion.

2.3 Free electron in a laser field: Volkov states

The problem of a charged particle in a laser field is one of the few quantum mechanical problems with an analytical solution. We start with the time-dependent Schrödinger equation in the length gauge:

$$i\frac{\partial\Psi(\mathbf{r},t)}{\partial t} = (-\frac{\triangle}{2} + \mathbf{r}\mathbf{E}(t))\Psi(\mathbf{r},t). \tag{2.5}$$

It is straightforward to verify that the following Volkov states are solutions of the time-dependent Schrödinger equation (2.4).

$$\Psi_V(\mathbf{r},t) = e^{i\mathbf{p}(t)\mathbf{r} - i\int_{-\infty}^{t} dt' \mathbf{p}^2(t')/2} \tag{2.6}$$

with

$$\mathbf{p}(t) = \mathbf{k} + \tilde{\mathbf{A}}(t). \tag{2.7}$$

$\mathbf{k}$ is the electron momentum in the absence of the electric field and $\tilde{\mathbf{A}}(t) = -\int_{-\infty}^{t}\mathbf{E}(t')dt'$. The Volkov states look like ordinary plane waves with a time dependent wave vector $\mathbf{p}(t)$. The integral in the exponent provides a term which is constant in time and space and act like an energy shift. This term depends quadratically on the amplitude of the field and is inverse proportional to the wavelength squared. This term is called the ponderomotive energy U_p and given by

$$U_p = \frac{I}{4\omega^2}. \tag{2.8}$$

The ponderomotive energy is the cycle-averaged kinetic energy which an electron gains because of the laser field.

2.4 Keldysh parameter

When an atom is placed in an intense laser field, an electron can be ionized either through a multiphoton or a tunneling mechanism. The distinction is based on the so-called Keldysh parameter

$$\gamma = \sqrt{I_p/(2U_p)}, \tag{2.9}$$

where I_p is the ionization energy and U_p is the ponderomotive potential. In the multiphoton regime, which is characterized by $\gamma \gg 1$, the resulting photoelectron spectra show the characteristic ATI peaks separated by the photon energy (DiMauro and Agostini [34], Agostini et al. [35]). With increasing laser intensity and wavelength the Keldysh parameter decreases. When γ is less than one, tunneling ionization dominates. In this regime the laser electric field distorts the atomic potential so that the electron can tunnel through the barrier. The corresponding electron spectra exhibit a continuous distribution (Mevel et al. [36], DiMauro and Agostini [37], Ammosov et al. [38], Bisgaard and Madsen [39], Perelomov et al. [40], Delone and Krainov [41]).

2.5 Strong Field Approximation

Solving the time-dependent Schrödinger equation numerically is straightforward, however, a time consuming task. For practical reasons it is therefore beneficial to have a simple model at hand. I have used in this thesis a model based on the strong-field approximation and only for the cases where it was possible we have compared our model results with a solution of the time-dependent Schrödinger equation. We find that many features of the ab-initio solutions can be understood within the strong-field approximation.

There is no general analytical solution to the Schrödinger equation for a charged particle with both the field of an attractive Coulomb potential and an electromagnetic field. The most common approximative analytical model is the Keldysh-Faisal-Reiss model (KFR) (Keldysh [8], Faisal [42], Reiss [43]) which has been extensively applied in atomic physics. Standard perturbation techniques are known to fail in the case of multiphoton ionization of atoms in a strong laser field. In particular, above-threshold ionization (ATI)

photoelectron peaks, produced when an atom has absorbed more photons than required to overcome the binding potential, cannot be explained by perturbation theory. Keldysh (Keldysh [8]) was the first one to formulate a nonperturbative approach to this problem on the assumption that the atomic potential can be neglected in the final state if the field is sufficiently strong. The final state can then be taken to be that of a free electron moving in a time- dependent classical field. Faisal and Reiss (Faisal [42], Reiss [43]) have carried Keldysh's approach further by applying time-dependent scattering theory. The Hamiltonian in length gauge,

$$H = \frac{\mathbf{p}^2}{2} + \mathbf{r}\mathbf{E}(t) + V(\mathbf{r}), \tag{2.10}$$

can be split up into three parts: the kinetic energy of the electron $\frac{\mathbf{p}^2}{2}$, the atomic core potential $V(\mathbf{r})$ and the atom-field interaction $\mathbf{r}\mathbf{E}(t)$. The wave function at time t can be written as

$$|\Psi(t)\rangle = U(t, t_0)|0\rangle, \tag{2.11}$$

where $|0\rangle$ is the initial atomic bound state. The propagator $U(t, t_0)$ contains the full Hamiltonian. Its equation of motion can be written in terms of the integral equation

$$U(t, t_0) = U_c(t, t_0) - i \int_{t_0}^{t} dt'' U(t, t'')\mathbf{r}\mathbf{E}(t'')U_c(t'', t_0), \tag{2.12}$$

with

$$U_c(t, t') = e^{-i \int_{t'}^{t} (H_0 + V(\mathbf{r}) dt''}, \tag{2.13}$$

where $H_0 = \frac{\mathbf{p}^2}{2}$. The amplitude for ionization with final momentum $\mathbf{k}$ is given by

$$\langle \mathbf{k}|\Psi(t)\rangle = -i \int_{-\infty}^{\infty} dt U_V(t, t'')\mathbf{r}\mathbf{E}(t'')U_c(t'', t_0)|0\rangle. \tag{2.14}$$

We have substituted the full propagator $U(t, t')$ in the last equation by the propagator of Volkov states, defined by

$$U_V(t, t') = e^{-i \int_{t'}^{t} (H_0 + \mathbf{r}\mathbf{E}(t'')) dt''}. \tag{2.15}$$

This approach is similar to the distorted-wave Born approximation. Normally in the perturbative expansion the time evolution operator U_c is substituted for U in the integral of Eq. (2.12). This approximation accounts only for a first-order process which in this case is a single photon absorption. In the distorted wave approximation, as shown above, the operator U_V is substituted instead in order to represent the *distorted* final state in the strong field regime, *i.e.* Volkov state. Since this is not exactly the first order perturbative expansion, this distorted wave partially includes the higher order processes. Therefore, as will be shown later, this SFA approximation can also present a multiphoton absorption. Thus the SFA model is a modified distorted-wave Born approximation and explicitly includes the fact that the ground state is only weakly perturbed by the laser field, so that the term $\mathbf{rE}(t)$ can be neglected before the ionization, however, once the electron is ionized the electron moves in the field of the laser and the core potential is neglected. Unlike ordinary perturbation theory for a weak laser field, the SFA improves as the field becomes stronger.

Central to the idea of the strong-field approximation (SFA) (Keldysh [8], Faisal [42], Reiss [43]) is the distinction between a region 'inside' the atom where atomic forces dominate and 'outside' where the laser forces dominate. Basically, the influence of the laser field is neglected, as long as the electron is bound, and once it is ionized, the atomic potential is neglected. With a few more approximations, an almost analytical solution of the atom in a strong laser field can be obtained.
The main approximations of the SFA model are:

1. The contribution to the evolution of the system of all bound states except the ground state can be neglected.

2. The depletion of the ground state can be neglected as well.

3. In the continuum, the electron can be treated as a free particle moving in the electric field, with no effect of the atomic potential.

Assumption (2) is valid only for intensities smaller than the saturation intensity. Otherwise, the depletion of the ground state has to be taken into account. Assumption (3) is non-questionable for negative ions, but is also valid for atoms, provided the field strength is large enough. It is important to

be aware of the regime of validity of these approximations. In general, they hold when the contribution of intermediate resonances is small and when the Keldysh parameter is smaller than one, i.e in the tunneling regime. However, I will present results in this thesis, which prove that even for a Keldysh parameter larger than one the SFA model is able to produce reliable results.

Since the SFA model is an important part of this thesis we will give an alternative derivation (Lewenstein et al. [13]). With the assumptions (1-3) the time-dependent wave function can be expanded as:

$$|\Psi(t)\rangle = e^{iI_p t}\left(a(t)|0\rangle + \int d^3\ \mathbf{k} b(\mathbf{k},t)|\mathbf{k}\rangle\right), \tag{2.16}$$

where $a(t)$ is the ground state amplitude and $b(\mathbf{k},t)$ are the amplitudes of the corresponding continuum states, $I_p > 0$ is the ionization potential. The free oscillations of the ground state with the frequency I_p have been factored out. Inserting this expansion in the time-dependent Schrödinger equation leads to the following differential equation for the amplitudes $b(\mathbf{k},t)$ (Lewenstein et al. [13]):

$$\dot{b}(\mathbf{k},t) = -i\left(\frac{\mathbf{k}^2}{2} + I_p\right) b(\mathbf{k},t) - E(t)\frac{\partial b(\mathbf{k},t)}{\partial \mathbf{k}_z} + iE(t)d_z(\mathbf{k}). \tag{2.17}$$

Here $d_z(\mathbf{k}) = \langle \mathbf{k}|z|0\rangle$ denotes the atomic dipole matrix element of the bound-free transition. In writing equation (2.17) we have neglected the depletion of the ground state, setting $a(t) = 1$ on the right-hand side. The entire information about the atom is thus contained only in the dipole matrix element and the ionization potential I_p. The equation 2.17 can be solved exactly and $b(\mathbf{k},t)$ can be written in the closed form,

$$\begin{aligned} b(\mathbf{k},t) &= i\int_{-\infty}^{t} dt' E(t') d_z(\mathbf{k} + \tilde{\mathbf{A}}(t) - \tilde{\mathbf{A}}(t')) \\ &\quad \times e^{-i\int_{t'}^{t} dt''(\mathbf{k}+\tilde{\mathbf{A}}(t)-\tilde{\mathbf{A}}(t''))^2/2 + I_p}, \end{aligned} \tag{2.18}$$

where

$$\tilde{\mathbf{A}}(t) = -\int_{-\infty}^{t} dt' \mathbf{E}(t') \tag{2.19}$$

is up to a factor of c the vector potential of the laser field. The value of $b(\mathbf{k}, t)$ is then the amplitude for the ionization of an electron with the final momentum $\mathbf{k}$. Equation (2.18) has a nice physical interpretation. The first factor in the integral is the probability amplitude for an electron to make a transition to the continuum at time t' with the canonical momentum $\mathbf{k}$. The electronic wave function is then propagated until the time t and acquires a phase equal to $\exp(-iS(\mathbf{k}, t, t'))$, where $S(\mathbf{k}, t, t')$ is the quasi-classical action. The effects of the atomic potential are assumed to be small between t' and t, so that $S(\mathbf{k}, t, t')$ actually describes the motion of an electron freely moving in the laser field. However, $S(\mathbf{k}, t, t')$ does incorporate some effects of the binding potential through its dependence on I_p.

The SFA has been applied in both length and velocity gauge with quantitatively conflicting answers (Bauer et al. [44]). However, it has been shown that the length-gauge form matches the exact numerical solution for the case of of a short-range binding potential, where the SFA is expected to be most accurate (Bauer et al. [45]). Additionally, in (Wiehle et al. [18]) is was reported, that for the case of negative fluorine ions exposed to a circularly polarized infrared pulse also the length gauge is the appropriate gauge to use, to obtain agreement with experimental data. From equation (2.18) it can be seen that the length gauge Hamiltonian puts emphasis on large distances from the atom, where the Volkov wave function is a good approximation. We go along this line and apply the SFA in the length gauge form as well.

2.6 Generalized Pseudospectral Method

In this section a numerical procedure to obtain a solution of the time-dependent Schrödinger equation is described (Tong and Chu [16, 17], Wang et al. [46], Telnov and Chu [47]). This method is applicable for atomic systems in intense, short laser fields with one active electron. We write the time-dependent Schrödinger equation in the following form:

$$i\frac{\partial}{\partial t}\Psi(\mathbf{r}, t) = (H_0 + V_{int})\,\Psi(\mathbf{r}, t), \tag{2.20}$$

where we separate the unperturbed atomic Hamiltonian H_0 and the time-dependent atom-field interaction $V_{int} = \mathbf{E}(t) \cdot \mathbf{r}$.

For the time-propagation we apply the split-operator technique:

$$\begin{aligned}\Psi(\mathbf{r}, t+\triangle t) &\simeq \exp\left(-iH_0\triangle t/2\right) \\ &\times \exp\left(-iV_{int}(\mathbf{r},\theta,t+\triangle t/2)\triangle t\right) \\ &\times \exp\left(-iH_0\triangle t/2\right)\Psi(\mathbf{r},t)+O(\triangle t^3)\end{aligned} \tag{2.21}$$

This expression is different from the traditional split-operator techniques, where H_0 is chosen to be the radial kinetic energy operator and V_{int} the remaining Hamiltonian depending on the spatial coordinates only. Equation (2.21) shows that the time propagation of the wave function from t to $t+\triangle t$ is achieved by three steps: First the wave function is propagated for a half-time step $\triangle t/2$ in the energy space spanned by H_0:

$$\exp\left(-iH_0\triangle t/2\right)\Psi(\mathbf{r},t) \equiv \Psi_1(\mathbf{r},t). \tag{2.22}$$

Then the wave function $\Psi_1(\mathbf{r},t)$ is transformed back to coordinate space and propagated for a time step $\triangle t$ under the influence of the atom-field coupling:

$$\exp\left(-iV_{int}(\mathbf{r},\theta,t+\triangle t/2)\triangle t\right)\Psi_1(\mathbf{r},t) \equiv \Psi_2(\mathbf{r},t) \tag{2.23}$$

Finally, the wave function $\Psi_2(\mathbf{r},t)$ is transformed back to the energy space spanned by H_0 and propagated for another half-time step $\triangle t/2$:

$$\exp\left(-iH_0\triangle t/2\right)\Psi_2(\mathbf{r},t) = \Psi(\mathbf{r},t+\triangle t). \tag{2.24}$$

To pursue the time-propagation, it is helpful to expand the total wave function in Legendre polynomials.

$$\Psi(r,\theta,t) = \sum_{l=0}^{l_{max}} g_l(r)P_l(\cos\theta), \tag{2.25}$$

where P_l stands for the Legendre polynomial of order l. The propagation in energy space (first step) can now be expressed as

$$\Psi_1(r,\theta,t) = \sum_{l=0}^{l_{max}} \exp\left(-iH_l^0\triangle t/2\right) g_l(r,t)P_l(\cos(\theta), \tag{2.26}$$

with

$$H_l^0 = -\frac{1}{2}\frac{d^2}{dr^2} + \frac{l(l+1)}{2r^2} + V(r). \tag{2.27}$$

Note that in equation (2.26) each partial wave function component g_l is propagated independently under H_l^0. The key step in the time propagation is to construct the operator

$$\exp\left(-iH_l^0 \triangle t/2\right), \tag{2.28}$$

through an accurate representation of H_l^0. First we need an appropriate grid discretization method for the eigenvalue problem:

$$H_l^0(r)\chi_l(r) = \epsilon\chi_l(r). \tag{2.29}$$

For atomic structure calculations involving the Coulomb potential, one typical problem associated with equal-spacing grid-methods is the Coulomb singularity at $r = 0$ and the long-range nature of the Coulomb potential. Generally, one truncates the semi-infinite domain $(0, \infty)$ into the finite domain $[r_{min}, r_{max}]$ to avoid the Coulomb singularity at the origin and the infinite domain. For this purpose, r_{min} must be chosen sufficiently small and r_{max} sufficiently large. This results in the need of a large number of grid points. Next, the domain $[r_{min}, r_{max}]$ is mapped on to the interval $[-1, 1]$ using a nonlinear mapping $r = r(x)$, followed by the Legendre pseudospectral discretization. This procedure allows for a denser grid near the origin. We use the mapping function

$$r(x) = K\frac{1+x}{1-x+\alpha} \tag{2.30}$$

where K and $\alpha = 2 \times K/r_{max}$ are mapping parameters. The introduction of nonlinear mapping usually leads to an non-symmetric eigenvalue problem and thus one has to deal with non-hermitian matrixes. Such undesirable features may be removed by the use of a symmetrization procedure. Thus by defining

$$\Phi_l(x) = \sqrt{r'(x)}\chi_l(r(x)), \tag{2.31}$$

one finds the transformed Hamiltonian possesses the following form:

$$H_l^0(x) = -\frac{1}{2}\frac{1}{r'(x)}\frac{d^2}{dx^2}\frac{1}{r'(x)} + V_l(r(x)) \tag{2.32}$$

where $V_l = l(l+1)/(2r^2) + V(r)$.

The central part of the pseudospectral method is to approximate the exact solution $\Phi_l(x)$ by a polynomial of order N. The polynomial cannot solve the differential equation for all x within the interval $[-1, 1]$. However, one can request that equation (2.29) is satisfied at the collocation points x_i. The approximate function $\Phi_l^N(x)$ can now be written as

$$\Phi_l^N(x) = \sum_{i=0}^{N} \Phi_l^N(x_i) g_i(x) \tag{2.33}$$

where $g_i(x)$ are the cardinal functions given by

$$g_i(x) = -\frac{1}{N(N+1)P_N(x_i)} \frac{(1-x^2)P_N'(x)}{x - x_i} \tag{2.34}$$

which satisfy the property $g_i(x_j) = \delta_{ij}$. In the Legendre pseudospectral method the collocation points are determined by the roots of the first derivative of the Legendre polynomial $P_N(x)$.

Discretizing the Hamiltonian operator leads to the following set of coupled linear equations:

$$\sum_{j=0}^{N} \left(-\frac{1}{2}(D_2)_{ij} + \delta_{ij} V(r(x_j)) \right) A_j = E A_i \tag{2.35}$$

The coefficients A_i are related to the wave function values at the collocation points as

$$A_j = \sqrt{r'(x_j)} \Psi(r(x_j)) \frac{1}{P_N(x_j)}. \tag{2.36}$$

The matrix $(D_2)_{ij}$, representing the second derivative with respect to r is given by

$$(D_2)_{ij} = \frac{1}{r'(x_i)} \frac{1}{(d_2)_{ij}}, \tag{2.37}$$

where $(d_2)_{ij}$ is the second derivative of the cardinal function $g_j(x)$ with respect to x.

$(D_2)_{ij}$ has the following explicit form:

$$\begin{aligned} (D_2)_{ij} &= \frac{1}{r'(x_i)} \frac{(N+1)(N+2)}{6(1-x_i^2)} \frac{1}{r'(x_j)}, \quad i = j \\ (D_2)_{ij} &= \frac{1}{r'(x_i)} \frac{1}{(x_i - x_j)^2} \frac{1}{r'(x_j)}, \qquad i \neq j \end{aligned} \tag{2.38}$$

The eigenvalues and eigenfunctions of H_l^0 will be denoted by $\epsilon_k(l)$ and $\chi_{ki}(l)$, respectively. The propagation of a given partial-wave function $g_l(r,t)$ under H_l^0 can now be expressed as

$$\left(\exp\left(-iH_l^0\triangle t/2\right)g_l(r)\right)_i = \sum_{j=1}^{N} S_{ij}(l)g_l(r_j); \tag{2.39}$$

where

$$S_{ij}(l) = \sum_k \chi_{ki}(l)\chi_{kj}(l)\exp\left(-i\epsilon_k(l)\triangle t/2\right). \tag{2.40}$$

In this thesis the pseudospectral method will be used to calculate energy spectra and angle-resolved momentum distributions for single ionization in a linearly polarized few-cycle pulse. The energy spectrum is obtained by projecting the wave function on a Coulomb wave with a certain energy. The final wave function can be expanded in atomic eigenstates:

$$\Psi(\mathbf{r},t) = \sum_{nl} a_{nlm}(t)\psi_{nlm}(\mathbf{r}) + \sum_l \int dE b_{lm}(E,t)\psi_{lm}(\mathbf{r},E), \tag{2.41}$$

where $\psi_{nlm}(\mathbf{r})$ and $\psi_{lm}(\mathbf{r},E)$ are the exact bound and scattering eigenfunctions. Since the magnetic quantum number m is conserved in a linearly polarized pulse, there is no need to sum over m. Now the probability distribution of an electron in the continuum can be written as a sum over the partial-wave contributions:

$$\frac{dP_E(t)}{dE} = \sum_l |b_{lm}(E,t)|^2. \tag{2.42}$$

For the computation of the angular distribution we project the electronic state on an outgoing Coulomb scattering wave function. Then the probability distribution of emission of an electron of energy $E = k^2/2$ at the time t propagating in direction $\hat{\mathbf{k}}$ is given by

$$\frac{d^2P_E(\mathbf{k},t)}{d\hat{\mathbf{k}}dE} = |\sum_l (-i)^l e^{i\delta_l} Y_{lm}(\hat{\mathbf{k}})b_{lm}(E,t)|^2. \tag{2.43}$$

Chapter 3

Energy Spectra for Single Ionization

In this chapter above-threshold-ionization (ATI) spectra for low-energy electrons will be presented. In recent years, the phenomenon of above-threshold ionization has been extensively studied with femtosecond laser pulses (Wiehle et al. [18], Nandor et al. [48], Cormier et al. [49], Assion et al. [50], Paulus et al. [51]). Above-threshold-ionization is a strong field phenomenon in which an atom absorbs more photons than necessary for ionization. The resulting photoelectron spectra exhibit features which can be described in terms of contributions of direct and rescattered electrons. The former reach the detector without recolliding with its parent ion, whereas the latter are driven back by the field and rescatter. From a simple classical analysis the maximum energies of the direct and rescattered electrons are $2U_p$ and $10U_p$, respectively. We mainly focus on the low energy part of the spectrum, i.e. the direct electrons. The overall characteristics of ATI spectra are peaks separated by the photon energy and shifted by the ponderomotive potential. In 1987 it was observed (Freeman et al. [52]) that the individual ATI peaks break up into a narrow fine structure, due to resonance enhancement in the ionization process produced by into resonance shifted bound states. Recently, in (Rodriguez et al. [53]) secondary peaks in the ATI spectrum have been reported and explained by the population of resonances in the ionization process, although the intensity is too low to induce any ponderomotive shift. In this case the broadband nature of the laser spectrum is responsible for

the excitation of the intermediate states. which are excited because of the broadband spectrum of the laser while the intensity is too low to induce any ponderomotive shift.

However, not only the wavelength also the intensity is not a well defined quantity for a short laser pulse. Therefore the concept of the ponderomotive potential, which is the cycle averaged kinetic energy of an electron in an oscillating field, is questionable in the few-cycle regime (Lindner et al. [54]). Since the field rises from zero to its peak value within a few femtoseconds each cycle has a correspondingly different ponderomotive potential. The question arises thus as to how well ATI spectra originating from intense few-cycle pulses resemble the well-known ATI structure by the longer pulses.

The electric field of the laser pulse can be written in the form $\mathbf{E}(t) = F_0\hat{\epsilon}a(t)\cos(\omega t + \varphi)$, with $\hat{\epsilon}$ the polarization vector, ω the carrier frequency and φ the carrier-envelope phase. The envelope function $a(t)$ is chosen to be

$$\sin^2\left(\frac{\pi(t+\tau/2)}{\tau}\right) \qquad -\frac{\tau}{2} < t < \frac{\tau}{2} \tag{3.1}$$

and zero elsewhere. Choosing an envelope function with a longer tail, for example a Gaussian, would be more realistic, however, because of computational reasons we chose the above envelope function.

To calculate the photoelectron energy spectra within the SFA approximation, we need to evaluate equation (2.18) for $t \to \infty$. This leads to the following ionization amplitude:

$$b(\mathbf{p}) \;=\; i\int_{-\infty}^{\infty} dt\; e^{i\phi_V(\mathbf{p},t)}\langle \mathbf{p}-\tilde{\mathbf{A}}(t)|H_L(t)|g\rangle_t \tag{3.2}$$

where the Volkov phase ϕ_V can be written as

$$\phi_V(\mathbf{p},t) = -\int_t^{\infty} dt' \frac{(\mathbf{p}-\tilde{\mathbf{A}}(t'))^2}{2}. \tag{3.3}$$

We have calculated the dipole matrix element $\langle \mathbf{p}-\tilde{\mathbf{A}}(t)|z|g\rangle$ using the energy scaled hydrogenic wave function. The corresponding matrix element for argon is

$$\langle \mathbf{p}|z|3p\rangle \propto \frac{-24a^2\left(-1+90a^2p_z^2-81a^4p^2(-p^2+6p_z^2)\right)}{(1+9a^2p^2)^5}, \tag{3.4}$$

	a1	a2	a3	a4	a5	a6
Argon	16.03862	2.007423	-25.54278	4.524663	0.9613848	0.4426447

Table 3.1: Parameters used for the model potential in equation (3.5).

where ionization happens from the 3p orbital. We only need to calculate the contribution for $m = 0$ since $m = \pm 1$ have a much smaller ionization probability. The parameter $a = 1/Z$ is scaled according to $2E_g n^2 = Z^2$. Although we use a scaled hydrogenic wave function to calculate the dipole matrix element we obtain, as shown in this and the next chapter, a good agreement with the TDSE calculation in the energy and angle-resolved momentum spectra. However, for sure a better agreement between TDSE and SFA will be found by including the exact dipole matrix element in the SFA calculation.

3.1 Effective model potential

For the numerical solution of the TDSE we have to specify the effective potential. We use a model potential of the following form (Tong and Lin [55])

$$V(r) = -\frac{1 + a_1 e^{-a_2 r} + a_3 r e^{-a_4 r} + a_5 e^{-a_6 r}}{r} \tag{3.5}$$

The parameters a_i are given in table (3.1).

The $a_i's$ are obtained by fitting the numerical potential calculated from the self-interaction free density functional theory. Furthermore the parameter a_3 is fine-tuned to make the ionization potential from the model potential in good agreement with the measured one. For large r, the argon and neon potential show the $-1/r$ Coulomb tail. For small r the effective potential exhibits a $-Z/r$ behavior, where Z is the nuclear charge.

3.2 Electron spectra for 400 nm

In the following we will compare the results from the numerical solution of the time-dependent Schrödinger equation, with the results obtained from the SFA

model. This comparison allows us to estimate the importance of the Coulomb potential and of intermediate resonances in the ionization process. However, the main motivation that lead to the results presented in this chapter was a certain substructure which we found in the ATI spectra (Wickenhauser et al. [14], Bardsley et al. [19]). We found that this substructure is caused by the shifting ponderomotive potential in the laser pulse and is typical for ionization with a short pulse.

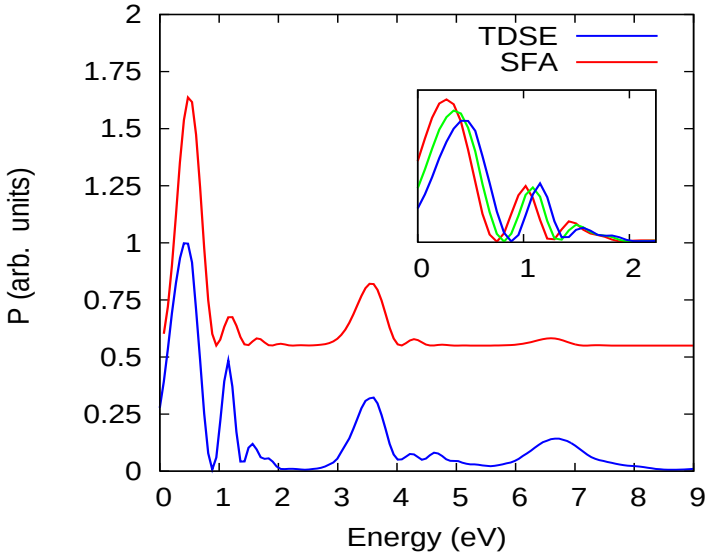

Figure 3.1: Photoelectron spectra of argon calculated by solving the TDSE and by using the SFA model. We have added a constant to the upper curve to distinguish the two lines more clearly. Furthermore, the SFA result has been normalized to the same peak height as the TDSE result, for better comparison. Each of the three ATI peaks is separated into a number of smaller peaks with varying amplitudes. Laser parameters are: $\omega = 400$ nm, $I = 1.7 \times 10^{14}$ W/cm^2. The pulse length (FWHM) is 10 fs. Inset: Photoelectron spectra in the region of the first ATI peak for three different intensities, $1.7, 1.75$ and 1.8×10^{14}W/cm^2, respectively, obtained by solving TDSE. These three intensities correspond to a ponderomotive shift of $2.55, 2.62$ and 2.70 eV, respectively. The peak positions shift closer to the threshold with increasing intensities.

We focus in this section on a wavelength of 400 nm which was relevant for

recent experiments at Kansas State University at the time when this research was performed. However, in the following sections we will also discuss the energy and momentum spectra for a wavelength of 800 nm which is the typical wavelength available for short-pulse experiments.

In Fig. 3.1 we present the photoelectron spectra obtained by the ab-initio solution of the TDSE (lower curve) and for comparison by using the SFA model (upper curve). Both spectra are normalized to the same peak amplitude. We simulate a 10 fs laser pulse with a carrier-wavelength of 400 nm and an intensity of 1.7×10^{14} W/cm^2. In general we observe a good agreement between the two calculations, as seen in Fig. 3.1. Three ATI peaks which are spaced by the photon energy $\omega = 3.1$ eV are visible in both spectra. On the right side each ATI peak breaks up into a number of smaller sub-peaks with varying amplitudes.

Although these sub-peaks in the ATI spectra look, at first, similar to Freeman resonances (Freeman et al. [52]), we prove that they are of a different nature. The inset in Fig. 3.1 shows the spectra in the neighborhood of the first ATI peak for three increasing intensities, $1.7, 1.75$ and 1.8×10^{14} W/cm^2, respectively, obtained by solving the TDSE. The overall structure of the spectra is identical for all three intensities, however, the peak positions differ. Apart from ionizing the atom, the laser field also induces an ac Stark shift to the atomic level. This shift increases the ionization potential by the ponderomotive energy, U_p. Because of energy conservation the energy of an ATI peak originating from ionization with absorbing n photons is given by

$$E = n\omega - (I_p + U_p), \tag{3.6}$$

where I_p is the ionization potential of the unperturbed atom and U_p is calculated from the peak laser intensity. According to this equation we can identify $(I_p + U_p)$ as the field-dressed ionization potential. Thus the fraction of an ATI peak originating from ionization at the peak intensity is shifted most to the left, since it observes the largest field-dressed ionization potential. Since the energy positions of all the sub-peaks in the ATI spectra move with changing intensity, they do not show the typical behavior of a Freeman resonance, where the energy position stays fixed (Freeman et al. [52], Gillen and VanWoerkom [56]) when the laser intensity is varied. Another proof of the non-resonant character of the small peaks is provided by a comparison of the TDSE calculation with the results obtained from the SFA model. All

main features from the numerical calculation, including ATI peaks, as well as sub-peaks, can be reproduced within the SFA model. In this model, besides the ground state, only the continuum states are included, therefore the small peaks can not originate from any intermediate resonances. Furthermore the similarity in the results between the two different calculations indicates that the effect of the long-range Coulomb force, which is not included in the SFA model, has only negligible influence on the substructure in the ATI spectrum for the laser parameters used in this calculation. Furthermore, we want to note that the presented spectra do not depend on the carrier envelope phase, as can be expected for a 10 fs laser pulse.

3.3 Role of the ponderomotive potential in the ionization process

In the following we show that the substructure in the ATI peaks is caused by the changing field-dressed ionization potential during the ionization process. It is significant for short, intense laser pulses and therefore a general feature which does not depend on the atomic target.

As seen from equation (3.6) the ponderomotive energy shifts the position of an ATI peak. Since in a few-cycle laser pulse the intensity changes rapidly in a relatively short time period, the contributions to ionization from different cycles of the pulse observe each a different ponderomotive potential and are thus not centered at the same energy. Therefore the ionization amplitudes from different cycles do not add up fully coherently while forming an ATI peak. The contribution coming from the region around the peak laser field is shifted most to the lower energy side compared to ionization from regions of the pulse with smaller intensity. These are shifted to the higher energy side. Since a laser with peak intensity of 1.7×10^{14} W/cm^2, as we have used for our simulations and which is a typical experimental value, has a ponderomotive energy of 2.55 eV at 400 nm compared to a spacing between the ATI peaks of 3.1 eV, this shift can not be neglected. For a better understanding we have a closer look at the SFA model. The term $\tilde{\mathbf{A}}(t)^2/2$ in the Volkov phase averaged over one cycle equals the ponderomotive potential and acts as a time dependent energy shift. To prove the assumption that the small peaks are caused by this time dependent shift we subtract the corresponding term

from the Volkov phase so that

$$\tilde{\phi}_V(\mathbf{p}, t) = -\int_t^\infty dt'(\frac{\mathbf{p}^2}{2} - \mathbf{p}\tilde{\mathbf{A}}(t')) \tag{3.7}$$

remains. Fig. 3.2 shows the results obtained with the SFA model when using $\tilde{\phi}_V$ as the phase factor in equation (2.18). All other parameters are the same as in Fig. 3.2. Obviously, all the substructure in the ATI spectrum disappears. The ATI peaks are shifted with respect to Fig. 3.2 since the ponderomotive shift is missing.

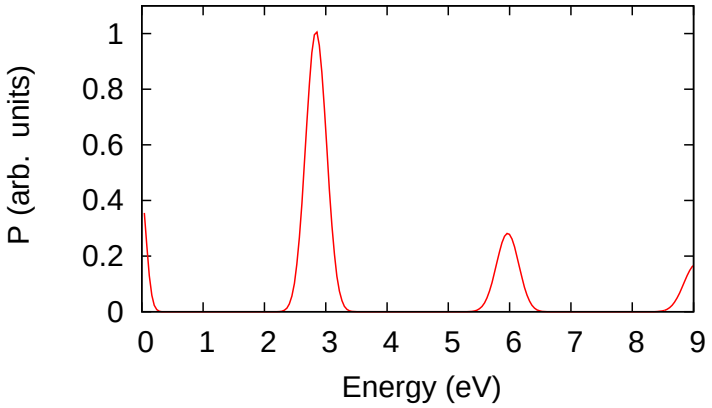

Figure 3.2: Photoelectron spectrum calculated using the same parameters as in Fig. 3.1 obtained with the SFA model, but with the redefined Volkov phase $\tilde{\phi}_V$ which does not include the ponderomotive energy shift. All subpeaks disappear from the spectrum. The peaks are shifted compared to 3.1 as a result of the missing ponderomotive energy.

In Fig. 3.3 we present the spectrum originating from ionization from only one optical cycle at three different positions in the laser pulse. This calculation was performed with the SFA model since in this model we can easily distinguish between ionization, which is described by the dipole matrix element, and the propagation of the ionized electrons which is represented by the Volkov phase factor. The three curves in Fig. 3.3a originate from ionization only during the intervals [0, T], [T, 2T] and [2T, 3T], respectively, where T = 1.33 fs is the laser period. (At time $t = 0$ in our simulation the laser pulse has reached its peak intensity.) After ionization we propagate each time until the pulse is over.

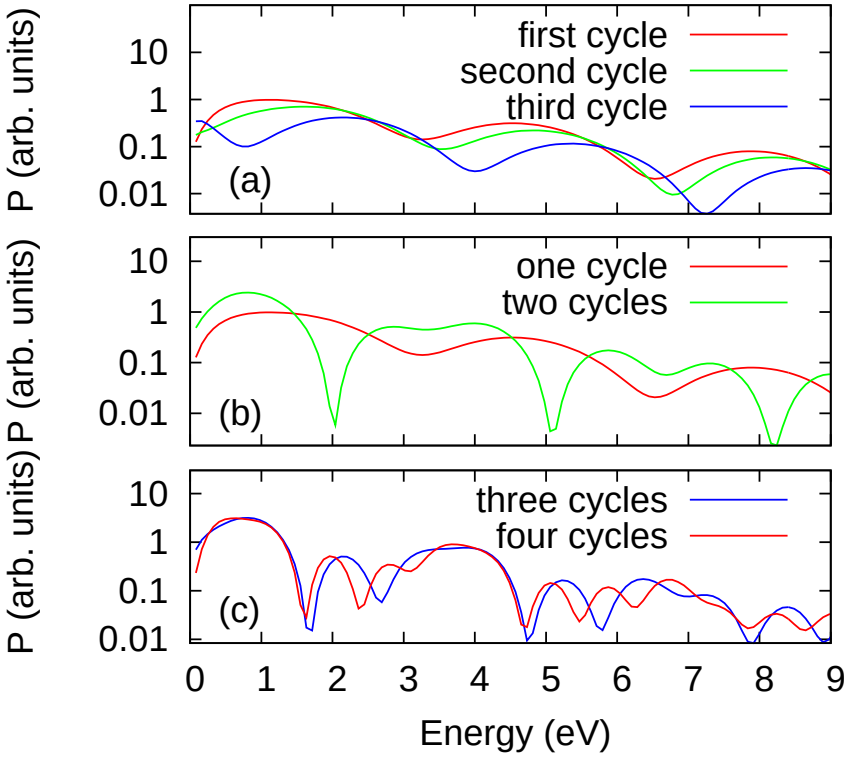

Figure 3.3: a) Spectra originating from ionization from one single optical cycle at three different periods of the laser pulse, [0, T], [T, 2T] and [2T, 3T], respectively. In contrast to Fig. 3.1 we have used here a logarithmic scale so that the smaller substructures are better visible. The contributions from the different cycles are shifted relatively to each other according to the different ponderomotive potential at the time of ionization. b) Spectra resulting from ionization through one, and two optical cycles, respectively, starting at the peak laser field. c) Spectra resulting from ionization through three and four optical cycles, respectively. The number of peaks in the ATI spectra increases with the number of laser cycles relevant for the ionization process. Calculations carried out within the SFA model.

Obviously, ionization from one optical cycle Fig. 3.3a is already enough to observe the typical ATI structure in the spectrum, though the peaks are broader than they will become after ionization from the whole pulse. The peak positions from the contributions of the different cycles are shifted according to the instantaneous field-dressed ionization potential at the time of release of an electron. Also visible is the decreasing probability for ionization from the different cycles. Fig. 3.3b and Fig. 3.3c show the spectrum from ionization of $t = 1, 2, 3$ and 4 optical cycles, respectively. While the absolute position and number of peaks obviously depends strongly on the phase with which the ionization amplitudes from the different cycles interfere, we note a general trend: the number of peaks increases with the number of cycles relevant for ionization and is therefore an indicator for the pulse length. Another interesting property of these peaks is presented in Fig. 3.4. In this figure we compare the energy positions of the different sub-peaks as a function of intensity. The peak positions have been determined from numerical solutions of the TDSE for the corresponding intensities. While the shift of the main peak agrees well with the ponderomotive potential calculated at the peak laser field, the shift of the smaller peaks is getting less, as clearly seen from their decreasing slopes.

The energy shift is a measure of the average intensity which is present during the ionization process which contributes most to a certain peak. Thus the decreasing shift follows approximately the envelope function of the laser pulse.

We have performed simulations for longer pulse durations. In both the numerical as well as the SFA model calculation we see an increase in the number of sub-peaks with the pulse duration. In the SFA model all sub-peaks remain separately visible, however, in the numerical calculation we observe a different trend. As the spacing between the various peaks becomes narrower with increasing pulse length, the intermediate regions begin to fill up. Since the main difference between the SFA model and the numerical calculation is the absence of the Coulomb potential in the former we suspect that the Coulomb force, which leads to a phase correction (Chirilă and Potvliege [57]) in equation (2.18), is responsible for this behavior.

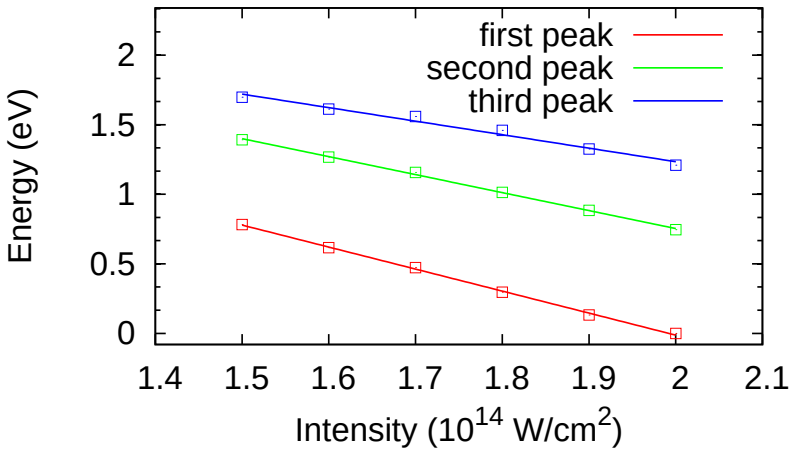

Figure 3.4: Energy positions of the three leftmost peaks in Fig. 3.2 as a function of peak laser intensity. The shift of the leftmost peak (lowest line) agrees well with the ponderomotive energy calculated with the peak laser intensity. The shifts of the following sub-peaks are smaller due to the smaller intensity the electrons experiences during the ionization process.

3.4 Electron spectra for 800 nm

In Fig. 3.5 the ATI spectrum for a 10 fs, 800 nm pulse is presented. Again we compare the TDSE calculation with the SFA model, though this time we do not observe a good agreement. The difference between the two calculations can be probably attributed to Freeman resonances which are not included in the SFA model calculation.

There are two reasons why this effect is more pronounced for 800 nm compared to the 400 nm case: Because of the smaller photon energy the number of photons participating in the ionization process is doubled and therefore the chance of hitting a resonance increases. Secondly, the ponderomotive potential at the same intensity is larger by a factor of four which makes it easier to shift an atomic state into resonance. Additionally, the ATI peaks are more closely spaced so that even within the SFA model calculation, the substructure is not so clearly visible in the 800 nm spectrum since the small peaks from one ATI peak could appear at the position of the next ATI peak. Therefore we can follow that the discussed substructure is also expected in the 800 nm case, however, it is almost impossible to separate it from Freeman

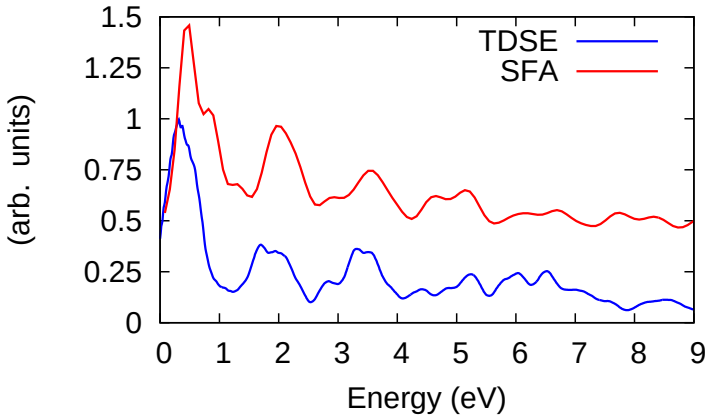

Figure 3.5: Photoelectron spectra of argon calculated by solving the TDSE and by using SFA model for a 10 fs, 800 nm pulse with 2×10^{14} W/cm^2 peak intensity. Compared to the 400 nm case in Fig. 3.1, the characteristic ATI peaks are still visible, but the spectrum shows a more complex structure. Differences between TDSE and the SFA calculation may originate from the presence of Freeman resonances in the former.

resonance contributions.

In this chapter, we have investigated the ATI spectra for argon by short laser pulses, both by solving the time-dependent Schrödinger equation and with the SFA model. We have observed and analyzed a certain class of subpeaks in the ATI spectra which is caused by the rapidly changing envelope of the laser field in a short pulse. The field-dressed ionization potential of the atom follows the rise and fall of the pulse envelope, and thus ionization at different optical cycles is mapped onto correspondingly different energies. A similar time to energy mapping in the laser field has been observed in experiments by the group of F. Krausz. In their case, an XUV attosecond pulse ionized the electron and a femtosecond laser pulse was used as a probe (Goulielmakis et al. [10], Drescher et al. [11]). In both experiments the intensity of the laser was about two orders of magnitude lower than the one used here so that the change in the ponderomotive potential was negligible. The change in the electron spectra in their experiments originates mainly from the factor $\mathbf{p}\tilde{\mathbf{A}}(t)$ in the Volkov phase. In contrast, we have reported on the influence of the time dependent ponderomotive potential on the ioniza-

tion process. The time to energy mapping occurs by shifting the field-dressed ionization potential of the atomic system itself on a femtosecond time scale.

Chapter 4

Angle-Resolved Momentum Distributions

In this chapter angle-resolved electron-momentum spectra will be presented. At the end of the chapter we address the issue of the double peak that was observed in the projection on the momentum parallel to the polarization direction (Rudenko et al. [20], Moshammer et al. [58]).

We focus in this chapter on laser parameters in the transition regime from tunneling to multiphoton ionization and analyze the change in the qualitative features of the 2D-momentum spectra with varying laser parameters. The electron spectra as well as their angular distributions are now considered to be well understood in the multiphoton regime for longer pulses, for example, see Ref. (Wiehle et al. [18]). However, recent measurements at higher laser intensities in the tunneling ionization regime revealed surprising results (Moshammer et al. [58]). In these experiments, the momentum distributions along the laser polarization direction were measured. According to the tunneling ionization theory one expects smooth spectra which peak at zero momentum. Instead, resonant-like peaks were found and a double-hump structure centered around $p_{||} = 0$ was observed (Moshammer et al. [58]).

We have performed quantum calculations of angle-resolved momentum distributions to get a more complete understanding of the ionization mechanism. Additionally, our calculations were motivated by recent experiments performed for a wavelength range from 400 nm to 800 nm (Maharjan et al. [21]).

Similar to the previous chapter, we obtained our results by solving the time-dependent Schrödinger equation numerically and by using the standard SFA, i.e., without introducing any corrections to account for the Coulomb potential. In the momentum spectra, we find "resonance-like" structures that can be attributed to multiphoton ionization on top of a smooth "background" due to tunneling ionization. However, sharp structures can also come from Freeman resonances for longer pulses and from incomplete constructive interferences for few-cycle pulses, as addressed in a recent paper (Wickenhauser et al. [14], Bardsley et al. [19]). Structures from the former are insensitive to the laser intensity, while caused by the latter change rapidly with the intensity. We illustrate the relative importance of tunneling vs multiphoton ionization features as the Keldysh parameter is varied. For the laser parameters used in our calculations we find that with the SFA model we can reproduce most features of the angle-resolved momentum distributions that appear in the TDSE calculation. However, we also point out which structures cannot be reproduced within the SFA approach.

We simulate a 10 fs (FWHM) laser pulse with a wavelength from 400 and 800 nm and a peak intensity in the range of 1.65 to 3.9×10^{14} W/cm^2. These laser parameters lie in the transition regime from multiphoton to tunneling ionization, with Keldysh parameters between 1.76 and 0.85.

4.1 Intensity dependence of the 2D momentum spectra

In Fig. 4.1 we present the angle-resolved momentum distributions for four different intensities, $1.7, 2.4, 3.2$ and 3.9×10^{14} W/cm^2, respectively, obtained by numerically solving the TDSE. The carrier wavelength is 400 nm, and the Keldysh parameters for the four intensities are 1.76, 1.48, 1.27 and 1.13. The carrier-envelope phase was set to zero. The horizontal axis in the plot is the momentum parallel to the laser field polarization and the vertical axis is the perpendicular momentum defined by $p_\perp = \sqrt{p_x^2 + p_y^2}$. ATI peaks appear as circles of increased ionization probability in the momentum distribution. It can be seen that the ionization probability is not constant on a given circle, but has maxima and minima. This structure reflects the parity and the dominant angular momentum of the emitted electrons at that particular

energy (Wiehle et al. [18], Arbo et al. [59]).

For the intensity of 1.7×10^{14} W/cm^2, Fig. 4.1a, three ATI peaks with alternating parity (seen from the node or antinode at $p_{||} = 0$) are visible. In the upper left and right corner of Fig. 4.1a a fraction of the fourth ATI peak is seen. Each ATI peak further breaks up into several sub-peaks with identical parities. For the first ATI peak three such sub-peaks can be seen. These sub-peaks have been explained by the shifting ponderomotive potential during the ionization process in the short pulse, which causes ionization at different times in the pulse not to add up fully coherently (Wickenhauser et al. [14], Bardsley et al. [19]).

For the first ATI peak in Fig. 4.1a we find $l = 1$ as the dominant angular momentum, as reflected by a central minimum flanked by two maxima in the angle-resolved spectrum. The second and third ATI peak have $l = 4$ and $l = 5$ as dominant angular momenta, respectively. Understanding the parity of the ATI peaks is straightforward. For the intensity 1.7×10^{14}W/cm^2, six photons are sufficient to ionize. However, at the intensity 2.4×10^{14}W/cm^2 Fig. 4.1b an additional photon is already needed for ionization. It can be seen that the first ATI peak starts to disappear below the threshold. The fraction which is still visible is attributed to the finite width of the ATI peak caused by the short pulse. For the intensity 3.2×10^{14}W/cm^2 the originally first ATI peak is hardly visible anymore and finally for $I = 3.9 \times 10^{14}$W/cm^2 the original second ATI peak has taken over the first position. This process is called channel switching. Since the valence orbital for argon is a p-orbital which has odd parity we can follow that the first ATI peak has also odd parity when an even number of photons is needed for ionization, e.g. see Fig. 4.1a, and even parity otherwise. The change in parity for two consecutive ATI peaks is clearly visible in Fig. 4.1. Thus the main features in Fig. 4.1 can be understood in terms of multiphoton ionization.

In Fig. 4.2 we present the results for the angle-resolved momentum distributions obtained from the SFA model for the same laser parameters as in Fig. 4.1, respectively. We observe a surprisingly good agreement with the full numerical result in Fig. 4.1. All ATI peaks with their corresponding substructures in the energy domain can be understood within the SFA. We see that the dominant angular momentum changes from one ATI peak to the next by an amount of 1, corresponding to the absorption of an additional photon. Additionally, the dominant angular momentum at a certain

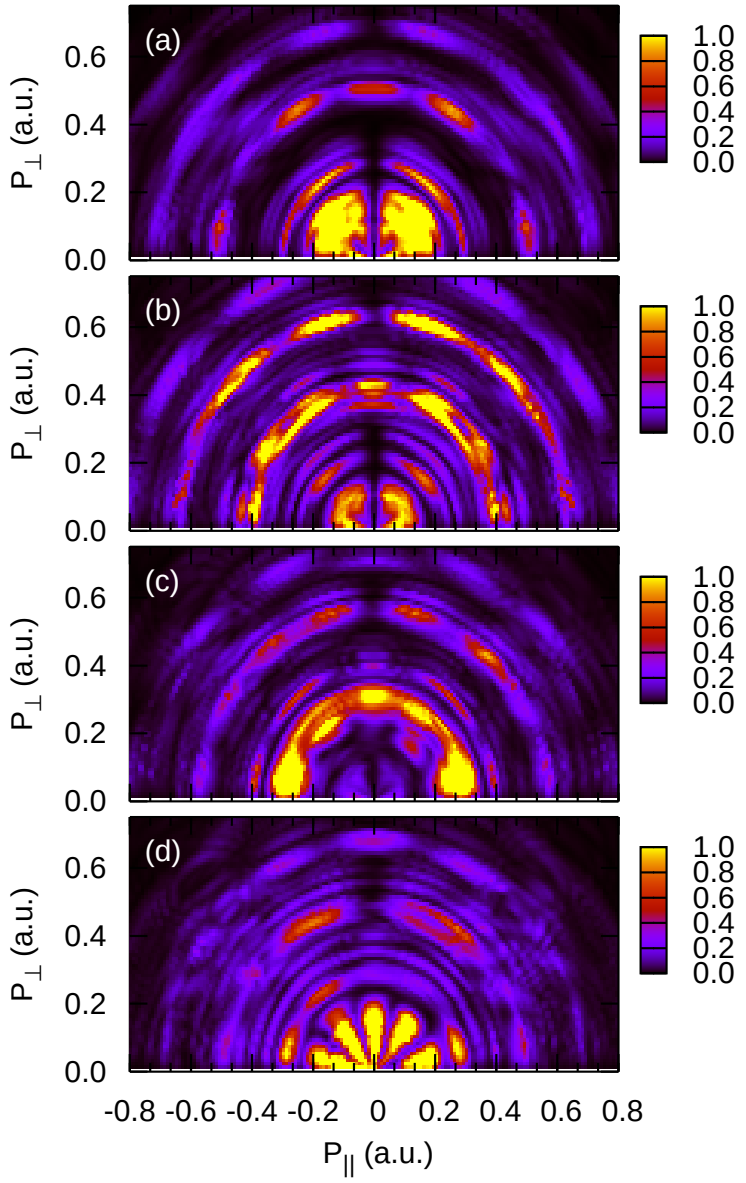

Figure 4.1: Photoelectron momentum distributions for argon calculated by solving the TDSE for four intensities, $1.7, 2.4, 3.2$ and 3.9×10^{14} W/cm^2, respectively, for a wavelength of 400 nm.

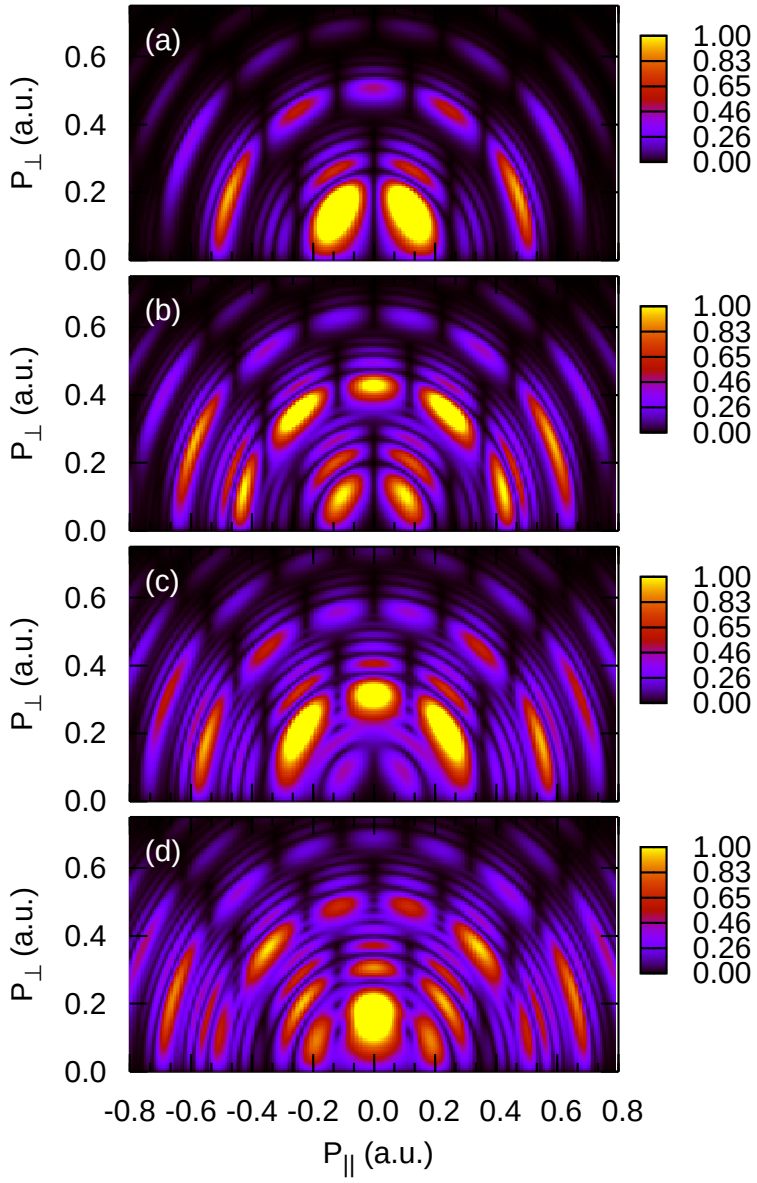

Figure 4.2: Photoelectron momentum distributions for argon calculated using the SFA model for four intensities, $1.7, 2.4, 3.2$ and 3.9×10^{14} W/cm^2, respectively, for a wavelength of 400 nm.

ATI peak can be reproduced in most cases within the SFA model. However, the angular momentum distribution may be affected by intermediate excited states in the ionization process as well as by the effect of the long-range Coulomb potential and is therefore impossible to predict exactly within the SFA approach. It is interesting to note the difference between the results from the two calculations. In the TDSE result the nodal lines in the momentum distribution of an ATI peak always fan out radially, while in the SFA model they are vertical. This leads to a sharper structure in the momentum projection in the SFA result as compared to the TDSE. This behavior of the SFA model can be understood straightforwardly. For a pulse of constant field strength F_0 acting from $0 < t < \tau$, the momentum dependent ionization amplitude $b(\mathbf{p})$ is proportional to the following sum

$$\sum_{n=0}^{\infty} f_n(p_{||}) \int_0^{\tau} dt e^{i(\mathbf{p}^2/2 - n\omega + I_p + U_p)t} \langle \mathbf{p} - \tilde{\mathbf{A}}(t)|z|g\rangle. \tag{4.1}$$

The function $f_n(p_{||})$ is given by

$$f_n(p_{||}) = \sum_{m+2j=-n\pm 1} i^m J_m(-\frac{p_{||}F_0}{\omega^2}) J_j(\frac{I}{8\omega^3}), \tag{4.2}$$

where the two sums run over all $-\infty < m, j < \infty$. J_m is a Bessel function of order m. Each term in the sum in Eq. (2) corresponds to a single ATI peak originating from the absorption of n photons which is located at the energy $\mathbf{p^2}/2 = n\omega - I_p - U_p$. The integral part of each term alone would result in a smooth momentum distribution. The nodal structure is caused by the prefactor $f_n(p_{||})$. Since $f_n(p_{||})$ depends only on $p_{||}$ and not on $p_\perp$ all nodal lines in the SFA calculation are vertical. While the difference between radial and vertical nodal lines is clearly seen in the ATI peak near threshold, it becomes smaller for higher ATI peaks.

4.2 Momentum distributions for 800 nm

In Fig. 4.3 we present the angle-resolved momentum spectra for a wavelength of 800 nm and two slightly different intensities of 1.65 and 1.8×10^{14} W/cm^2, corresponding to $\gamma = 0.89$ and 0.85, respectively. First we note the background continuum is much larger, as compared to Fig. 4.2. This is consistent

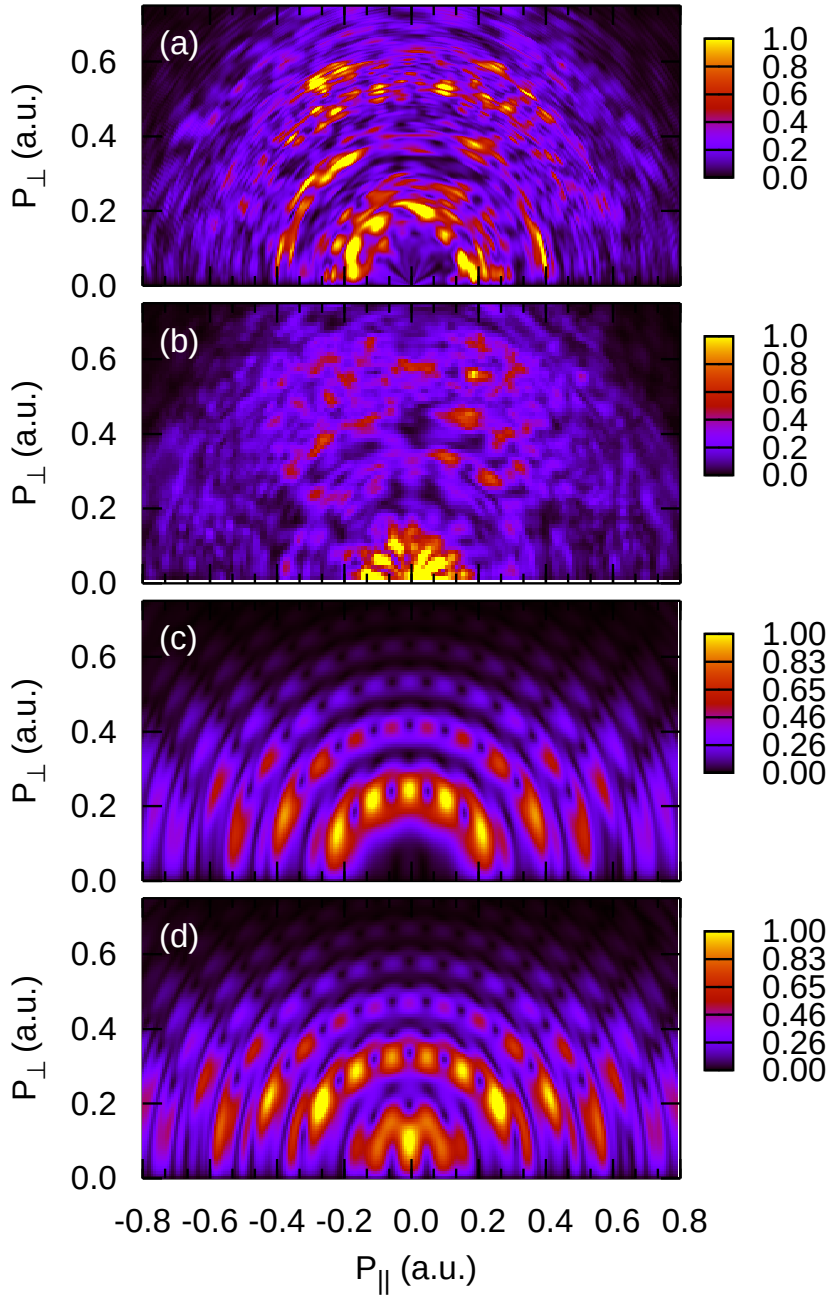

Figure 4.3: (a) and (b): Photoelectron momentum distributions for argon calculated using the TDSE for the intensities, 1.65 and 1.8×10^{14} W/cm^2, respectively, for a wavelength of 800 nm. (c) and (d): Photoelectron momentum distributions for argon calculated using the SFA model for the same parameters as (a) and (b), respectively.

with the smaller Keldysh parameter which means that tunneling ionization becomes more dominant. However, even in this regime the ATI peaks are visible, but the different peaks become now hard to distinguish. Figs. 4.3(a,b) are obtained with the full numerical solution of the TDSE, while Figs. 4.3(c,d) were calculated with the SFA model. Again it is visible that only the TDSE result shows the radial nodal lines in the momentum spectra, whereas in the SFA calculation the nodal lines are vertical. In Fig. 4.3a the first ATI peak is a photon energy away from threshold. For Fig. 4.3b the intensity was increased by an amount so that the first ATI peak is now close to threshold. Since for 800 nm the spacing between two ATI peaks is only ~ 1.55 eV, compared to 3.1 eV for 400 nm, a small increase in intensity, here it is less than 10%, is sufficient to move the position of an ATI peak by one unit of photon energy. At the end of this chapter we will show how the position of an ATI peak shapes the structure of the momentum projection on the polarization direction.

4.3 Wavelength dependence of the 2D momentum spectra

In Fig. 4.4 angle-resolved momentum spectra for four different wavelengths, 450, 500, 540 and 580 nm, respectively, are presented. The increase in wavelength was chosen so that each time an additional photon is needed for ionization. Therefore the parity of the ATI peaks alternates with the increase in wavelength. Together with the 400 nm case from Fig. 4.1a we observe that the dominant angular momentum for the first ATI peak changes with the increase of the wavelength from 1 to 4, 5, 2 and again 5. In the SFA model we see a more monotonic change in the dominant angular momentum, which indicates that the angular-momentum distribution obtained with the TDSE is influenced by contributions from resonances in a non-trivial way. However even with the TDSE calculation we see that, on average, the dominant angular momentum increases with the number of photons needed for ionization. The Keldysh parameters for Fig. 4.4 are 1.56, 1.41, 1.30 and 1.21, respectively.

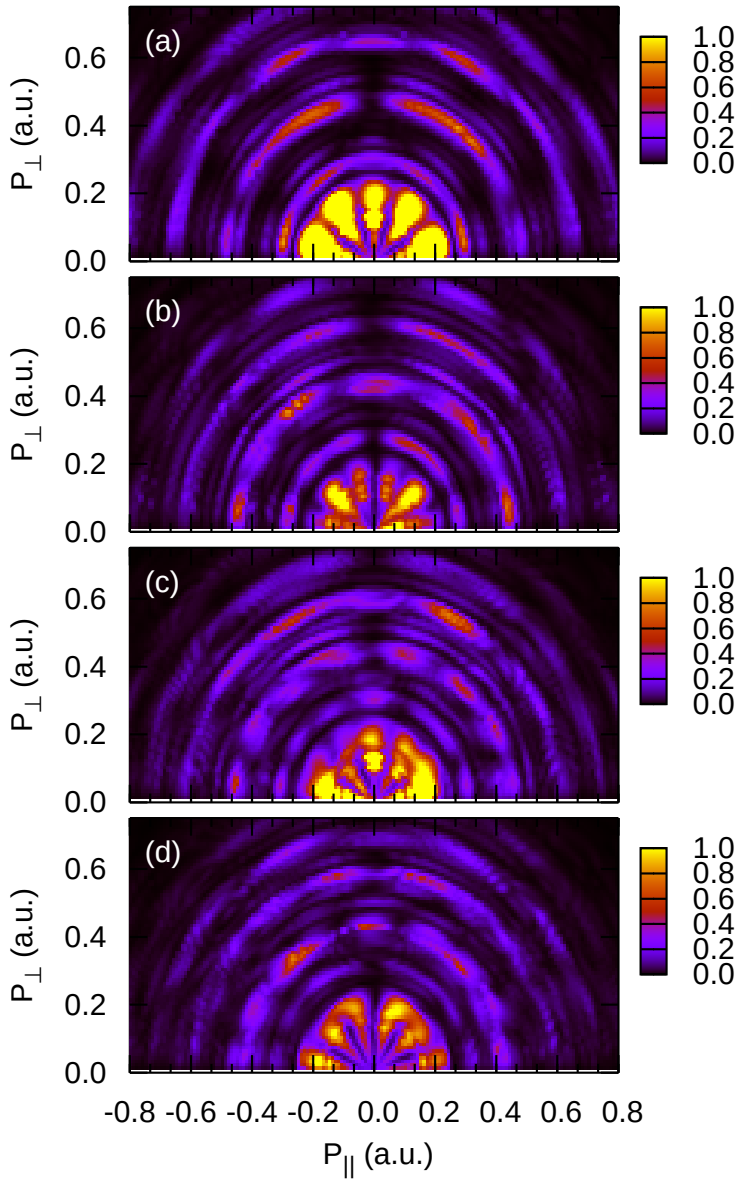

Figure 4.4: Photoelectron momentum distributions for argon calculated using the TDSE for the wavelengths $440, 500, 540$ and 580 nm, respectively for a peak intensity of 1.7×10^{14} W/cm^2.

4.4 Projection on the momentum parallel to the polarization direction

In recent experiments (Rudenko et al. [20], Moshammer et al. [58]) a double-hump structure was found in the momentum projection on the polarization direction. This double-hump structure was first attributed to a rescattering process, based on an earlier quasi-classical calculation (Chen and Nam [60]). Subsequently, based on another semi classical calculation, it was attributed to the effect of the Coulomb potential on the outgoing electron (Dimitriou et al. [61]). Experimentally, these structures were explained by Freeman resonances (Rudenko et al. [20]). In Ref. (Faisal and Schlegel [62]) they were considered to be evidences of multiphoton features in the tunneling regime. It was emphasized that the Coulomb interaction between the electron and the ion core is essential, and that Coulomb-Volkov states should be implemented in the SFA model. We have analyzed this structure and find that for the laser parameter used in our simulation the Coulomb potential is not relevant for the formation of the double-peak structure. The double-peak structure seems to be determined by the parity and the position of the first ATI peak (Faisal and Schlegel [62]).

In Figs. 4.5(a,b) we present the projection on the momentum parallel to the polarization direction for the SFA as well as from solving the TDSE for a wavelength 400 nm. The result from the SFA calculation is normalized to the same maximum peak as the TDSE result. We note that it has been stated in (Chirilă and Potvliege [57]) that the total ionization probability of a model based on SFA is too small and can be improved by multiplying the Volkov state with a correction factor which accounts for tunneling (Krainov and Shokri [63]). However, we do not include this factor since we intend to compare our TDSE calculation with a model which does not include any effect of the Coulomb potential. In Fig. 4.2c, we clearly see a dip in both calculations. This allows us to conclude that for these laser parameters the dip in the momentum projection is not caused by the effect of the Coulomb force. Additionally, from the good agreement we can estimate that the effects of the Coulomb potential and of intermediate resonances are small, at least in affecting the shape of the projected momentum distributions. For longer pulses, however, we expect the electron spectra and the momentum distribu-

tions are strongly influenced by Freeman resonances (Wiehle et al. [18]). In comparing Fig. 4.2c to Fig. 4.2d, we note that the latter has a larger smooth background. We can attribute this background to tunneling ionization which increases rapidly with higher laser intensity, or with smaller γ.

The 2D momentum distribution clarifies the behavior of the momentum projection in Figs. 4.5(a,b). In Fig. 4.5a, the first ATI peak has the highest amplitude and has odd parity, thus the momentum projection shows a dip in the middle with a maximum on either side. On the contrary, for the intensity 3.9×10^{14} W/cm^2, the momentum projection has a clear peak at $p_{||} = 0$, reflecting the even parity nature for the first ATI peak, since one more photon is needed for ionization.

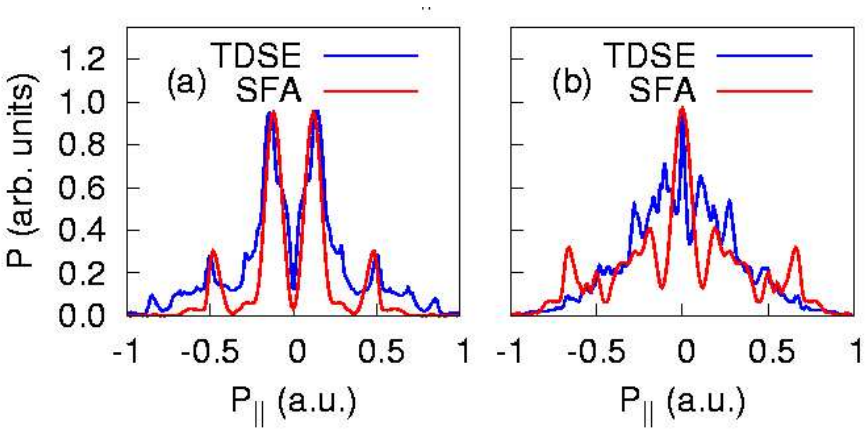

Figure 4.5: Comparison of the parallel momentum distributions between the TDSE result and the SFA calculation for the intensities, 1.7 and 3.9×10^{14} W/cm^2 and a wavelength of 400 nm, respectively.

For 800 nm we observe a different behavior. We see both a dip and a peak in Figs. 4.6(a,b) for even parity of the first ATI peak. Thus the projection on the parallel momentum is not dominated by the parity of the first ATI peak anymore. Moreover, the dip in the projected spectra changes to a central peak with a less than 10 percent increase in intensity. For Fig. 4.6b, the first ATI peak is close to threshold, for Fig. 4.6a it is about a photon energy away. Therefore we conclude that in the tunneling regime the position of the first ATI determines whether a peak or a dip is observed at the center of the momentum projection in agreement with (Faisal and Schlegel [62]).

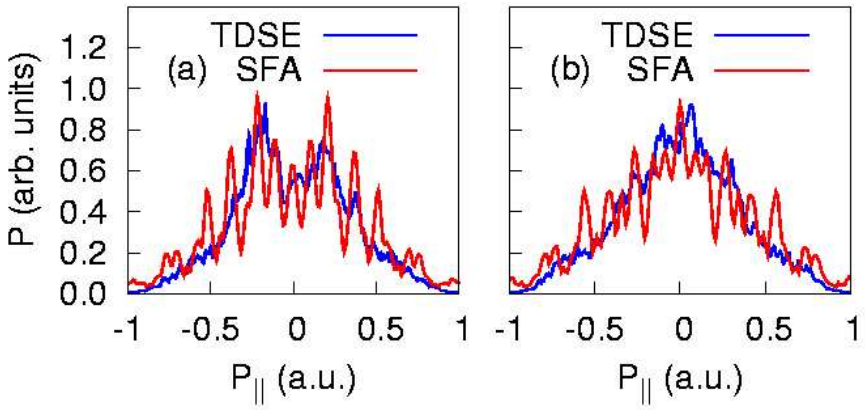

Figure 4.6: Comparison of the parallel momentum distributions between the TDSE result and the SFA model for the intensities, 1.65 and 1.8×10^{14} W/cm^2 and a wavelength of 800 nm, respectively.

4.5 Comparison with experiment

How to use the present theoretical results to explain existing experimental data? To begin with, most of the experimental data were taken with longer pulses, about 25-50 fs, and the finite size of the focal volume must be considered in a comparison. For 400 nm, general agreement between our calculation and experimental data (Maharjan et al. [21]) has been found, both in the projected momentum distribution and the main features in the 2D spectra. Since each ATI peak is 3.1 eV apart, it appears that the volume effect does not wash out the sharp features. For 800 nm, each ATI peak is separated only by 1.55 eV, and the sharp structures predicted in the theory are not expected to be observed after the volume integration. The position of a Freeman resonance, on the other hand, is rather insensitive to the laser intensity and thus can survive the volume effect. Therefore we agree that the structures observed in (Rudenko et al. [20], Moshammer et al. [58]) are likely coming from Freeman resonances. Whether the projected momentum spectra have a peak or a dip at $p_{||} = 0$ depends on whether a dominant resonance peak is close to the threshold or not.

In this chapter, we have investigated the 2D momentum spectra for above

threshold ionization of argon with a few-cycle laser pulse. Because of the absence of the smooth background in the multiphoton regime the parity and the dominant angular momentum of the first ATI peak determine the shape of the momentum projection. We have presented an example in the multiphoton regime where the dip in the momentum projection is caused by an odd parity of the first ATI peak. In the tunneling regime we support the results from (Faisal and Schlegel [62]) that the position of the first ATI peak determines whether a peak or a dip is seen in the momentum projection.

Chapter 5

Theoretical Description of a Fano Resonance

In this chapter the theoretical background for laser-dressed autoionization will be developed (Lambropoulos and Zoller [24], Agarwal et al. [64], Zakrzewski [65], Armstrong et al. [66], Alber and Zoller [67], Zhao and Lin [68]). We study a pump-probe scheme, where an attosecond pump pulse is used to excite a resonant state and an additional optical probe laser pulse samples the ionization process. In contrast to the previous chapters, where we have treated the ionization process with one-active electron, we will consider now the case that the laser pulse excites a resonant state which then decays due to electron-electron interaction. We focus on the case of an autoionizing decay, were an electron can be ionized via two paths leading to the same final kinetic energy. These two paths interfere and cause the characteristic asymmetric spectral profile. This profile is called a Fano resonance (Fano [22]). Since ab-initio solutions of the time-dependent Schrödinger equation are too tedious for this problem, we start from an effective one-electron problem and solv this within the strong field approximation. The atomic model that we consider consists of a ground state $|g\rangle$ and a resonant state $|r\rangle$ embedded in a structureless continuum $|E\rangle$, Fig. 5.1. The resonant state lies above the ionization threshold of the field-free Hamiltonian. We study its time evolution under the influence of an attosecond high-frequency low intensity pump pulse which initiates the autoionization process and a low-frequency high intensity probe pulse. The total Hamiltonian of the system therefore consists of the

following terms

$$H(t) = H_0 + H_{CI} + H_{XUV}(t) + H_{probe}(t), \tag{5.1}$$

with the atomic Hamiltonian $H_0 + H_{CI}$, where H_0 is the single configuration Hamiltonian and H_{CI} is the residual configuration interaction. H_{XUV} and H_{probe} describe the interaction of the atom with the XUV (extreme ultraviolet) pump pulse and the probe pulse in dipole approximation, respectively.

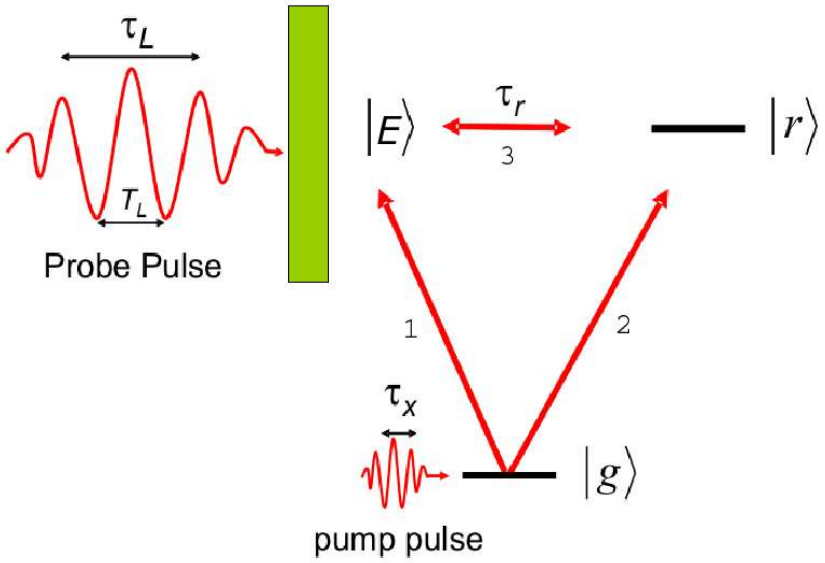

Figure 5.1: Schematic representation of the time-resolved autoionization process. Excitation with the pump pulse opens two interfering paths from the ground state to the continuum (compare Fig. 6.2). Arrival in the continuum is monitored by the probe pulse.

The resonant state $|r\rangle$ and the near-degenerate continuum $|E\rangle$ are coupled by the configuration interaction H_{CI}. Because of this interaction neither the continuum nor the resonant state are exact eigenstates of the atomic Hamiltonian. The diagonalization of the Hamiltonian is the cornerstone of Fano's treatment of the autoionization process within the framework of stationary states suitable for time-integral observations (Fano [22]).
These Fano states $|\Psi_E\rangle$ can be written as

$$|\psi_E\rangle = \frac{\sin(\Delta(E))}{\pi V_E}|\phi_E\rangle - \cos(\Delta(E))|E\rangle, \tag{5.2}$$

with

$$|\phi_E\rangle = |r\rangle + PP \int dE' \frac{V_{E'}}{E - E'} |E'\rangle. \tag{5.3}$$

The coupling matrix element between continuum and resonance is denoted by $V_E = \langle E|H_{CI}|r\rangle$ and PP denotes the principal part of the integral.

Unlike to Fano's treatment we are interested in the time dependence of autoionization. Therefore we solve the time dependent Schrödinger equation for which a formal solution can be written as

$$|\psi(t)\rangle = \hat{T} e^{-i\int_{-\infty}^{t} H(t')dt'} |\psi(t=-\infty)\rangle \;=\; U(t,-\infty)|g\rangle\,. \tag{5.4}$$

We solve Eq. (5.4) under the simplifying assumptions:
a) The weak XUV pulse is treated in first order perturbation theory and we neglect the influence of the pump pulse on the autoionization after the excitation process. This is justified because of the low intensity of this pulse compared to the probe pulse ($I_{XUV}/I_{probe} \sim 10^{-3}$).
b) We neglect the influence of the probe pulse on the resonant and the ground states, which would primarily lead to an energy shift of both the resonance and the ground state energies. The photon energy of the probe pulse is about 1.6 eV and therefore too small to cause any one-photon transition. Moreover, at moderate intensities ($I_{probe} \sim 10^{12}$ W/cm^2) ATI contributions can be neglected. The ponderomotive potential of the probe laser is 0.06 eV.
c) The emitted electron propagates in the continuum as a free particle thereby neglecting the core potential contained in H_0. This assumption is valid because the resonance energy lies tens of eV above the threshold.
Under the assumption a) Eq. (5.2) can be reduced to

$$|\psi(t)\rangle = -i \int_{-\infty}^{t} dt' \tilde{U}(t,t') H_{XUV}(t')|g\rangle_{t'}. \tag{5.5}$$

The propagator $\tilde{U}(t,t')$ contains now only H_0, the probe pulse H_{probe}, and the configuration interaction H_{CI}, but not H_{XUV}. Its equation of motion can be written in terms of the integral equation

$$\tilde{U}(t,t') = U_{probe}(t,t') - i \int_{t'}^{t} dt'' U_{probe}(t,t'') H_{CI} \tilde{U}(t'',t')\,, \tag{5.6}$$

with

$$U_{probe}(t,t') = e^{-i\int_{t'}^{t}(H_0 + H_{probe}(t''))dt''}$$

which provides a convenient starting point incorporating the additional approximations (b and c). Defining the propagator of Fano states as

$$U_F(t,t') = e^{-i\int_{t'}^{t}(H_0+H_{CI})dt''}\,, \tag{5.7}$$

the approximation b) allows to express Eq. (5.6) in terms of U_F as

$$\tilde{U}(t,t') \approx U_{probe}(t,t') - i\int_{t'}^{t} dt'' U_{probe}(t,t'')H_{CI}U_F(t'',t')\,. \tag{5.8}$$

The time-dependent amplitude for ionization $\langle E|\Psi(t)\rangle$ follows from Eq. (5.5) when we take into account the coherent excitation by the XUV pulse,

$$H_{XUV}(t')|g\rangle_{t'} = \int dE\ a_E(t')|E\rangle + a_r(t')|r\rangle\,, \tag{5.9}$$

with $a_E(t')$ and $a_r(t')$ being the time-dependent dipole transition amplitude to the continuum and the resonant states, respectively. Inserting Eqs. (5.8) and (5.9) into (5.5) yields

$$\begin{aligned}\langle E|\psi(t)\rangle \;=\; & -i\int_{-\infty}^{t} dt' \int d\tilde{E}\langle E|U_{probe}(t,t')|\tilde{E}\rangle a_{\tilde{E}}(t') \\ & -\int_{-\infty}^{t} dt' \int_{t'}^{t} dt'' \int d\tilde{E}\langle E|U_{probe}(t,t'')H_{CI}U_F(t'',t')|\tilde{E}\rangle a_{\tilde{E}}(t') \\ & -\int_{-\infty}^{t} dt' \int_{t'}^{t} dt''\langle E|U_{probe}(t,t'')H_{CI}U_F(t'',t')|r\rangle a_r(t').\end{aligned} \tag{5.10}$$

Eq. (5.10) can be further simplified by making use of assumption c) which implies the replacement

$$U_{probe}(t,t')|E\rangle = e^{-i\Phi_V(p,t,t')}|E(t,t')\rangle, \tag{5.11}$$

where $\Phi_E(t,t')$ is the Volkov phase, $\Phi_V(p,t,t') = \int_{t'}^{t} dt'' E(t'',t')$, with $E(t'',t') = \frac{(p+\tilde{A}(t'')-\tilde{A}(t'))^2}{2}$.
We thus arrive at

$$\begin{aligned}\langle E|\psi(t)\rangle \;=\; & -i\int_{-\infty}^{t} dt' e^{i\Phi_V(p,t',t)} a_{E(t',t)}(t') \\ & -\int_{-\infty}^{t} dt' \int_{t'}^{t} dt'' \int d\tilde{E} e^{i\Phi_V(p,t'',t)} V_{E(t'',t')}\langle r|U_F(t'',t')|\tilde{E}\rangle a_{\tilde{E}}(t') \\ & -\int_{-\infty}^{t} dt' \int_{t'}^{t} dt'' e^{i\Phi_V(p,t'',t)} V_{E(t'',t)} e^{-\frac{\Gamma}{2}(t''-t')-iE_r(t''-t')} a_r(t').\end{aligned} \tag{5.12}$$

The three terms in Eq. (5.12) represent different coherent pathways to the continuum final state $|E\rangle$ (see Fig. 6.2): the first two terms of Eq. (5.12) describe the direct excitation consisting of the transition from the ground state to the Volkov continuum (Fedorov [69]) in the absence of the resonance (first term) modified by a correction term due to interactions with the resonance (second term). The latter signifies virtual transitions from the continuum to the resonance and back to the continuum. The third term describes indirect transitions to the continuum via the resonant state $|r\rangle$.

Chapter 6

Excitation of an isolated Fano Resonance

In this chapter the time-evolution of an autoionizing decay initiated by an attosecond pulse will be studied. We note that a similar study has been done in (Zhao and Lin [68]). A prototype case for the coherent dynamics in a non-stationary system is the excitation of a Fano resonance. Fano line shapes are a ubiquitous feature of resonance scattering when the continuum can be accessed both directly and indirectly by way of a quasi-bound state embedded in the continuum (autoionization). Fano line shapes have been observed in the spectrum of time-integral measurements in a variety of phenomena including photo absorption in quantum well structures (Faist et al. [70]), scanning tunnel microscopy (Madhaven et al. [71]), and ballistic transport through quantum dots ("artificial atoms") (Göres et al. [72]). Interest in observing and analyzing Fano profiles is stimulated by their high sensitivity to the details of the scattering process, in particular the degree of transient coherence in the scattering system. Observing the non-stationary coherent dynamics by exciting a Fano resonance using an ultrashort pulse has, so far, not yet been attempted, most likely because of the challenging time scales involved. Interferences between different coherently excited autoionizing resonances have, however, been observed indirectly in ion-atom collisions where the decay can be monitored via the velocity dependence of the energy-shifted spectrum of the autoionizing electron due to the Coulomb field of the receding ion (Burgdorfer and Morgenstern [73]). With the avail-

ability of sub-fs XUV pulses with $\tau_X \approx 250$ as and the attosecond streak camera technique (Drescher et al. [11], Itatani et al. [74], et al. [75]) observation of coherent excitation of inner-shell processes appears to be within reach. In the following we present first results of our exploratory study for a generic model system tailored with potential atomic systems such as the lanthanides (Dzionk et al. [76]) in mind.
We first look at the time-integral profile. Near the resonance energy the emission spectrum can be parameterized by (Fano [22])

$$P(\epsilon) = \frac{(q+\epsilon)^2}{1+\epsilon^2} \tag{6.1}$$

with

$$\epsilon = \frac{E - E_r - \delta E}{\Gamma/2}, \tag{6.2}$$

where $\Gamma = 1/\tau_r$ is the inverse lifetime of the resonance. The quantity δE is a shift of the resonance position and depends quadratically on V_E. If this matrix element is only weakly energy dependent, this shift is small and can be neglected (Eichmann et al. [77]).

The Fano asymmetry parameter q is given by

$$q = \frac{\langle \Phi_{E_r} | T | g \rangle}{\pi V_{E_r} \langle E_r | T | g \rangle}, \tag{6.3}$$

where T is the transition operator for the excitation. This parameter is a measure for the relative importance of the direct transition from the ground state to the continuum as compared to the transition via the resonant state.

In Fig. 6.1 the spectral line shapes near the resonance energy for different Fano parameters q are presented. For negative q the scale of the abscissae has to be reversed. This figure was taken from (Fano [22]). The interference of the discrete autoionizing state with the continuum gives rise to the characteristically asymmetric peaks in the excitation spectra. Only for the two special cases of $q = 0$ and for $q = \infty$ is the spectrum symmetric around the resonance energy.

The central quantities in the following are the time-differential ionization probabilities

$$P(E,t) = |\langle E | \Psi(t) \rangle|^2 \tag{6.4}$$

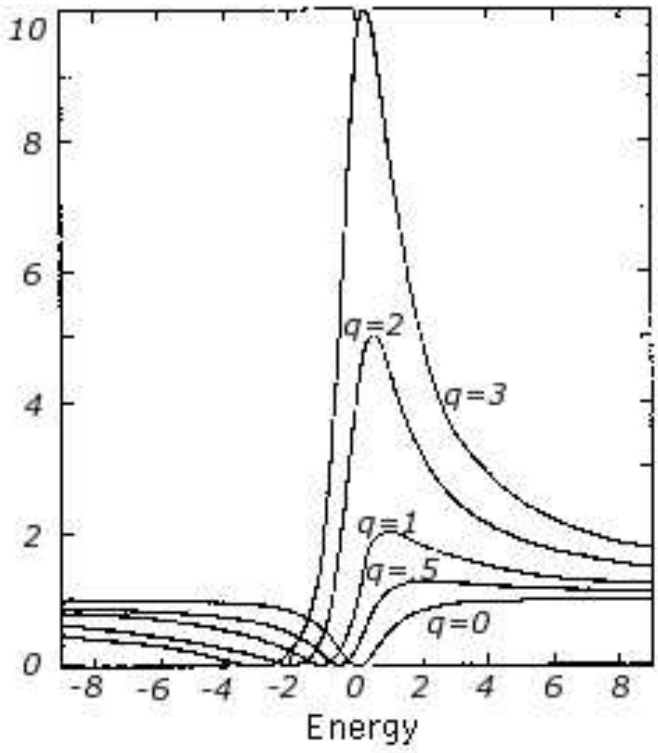

Figure 6.1: Spectral line shape near the resonance energy for different Fano parameters q. For negative q the scale of the abscissae has to be reversed. This figure was taken from (Fano [22]). The line shape for $q = 0$ is called a window resonance. For all other Fano parameters $0 < q < \infty$ the line shape is asymmetric.

as well as time-integral probabilities

$$P(E) = \lim_{t\to\infty} P(E,t). \tag{6.5}$$

The latter represents a standard emission spectrum of a Fano resonance in the limit that the influence of the probe pulse can be neglected. The time-resolved probability $P(E,t)$ is not directly accessible experimentally. Instead, the spectrum $P(E)$ can be recorded. In the next chapter we will analyze how the spectrum is changed by the probe laser pulse.

Fig. 6.2 shows $P(E)$ in the absence of the probe laser pulse for the different ionization channels. Fig. 6.2a represents the ionization spectrum in the absence of the resonance. The width of the spectrum is given by the inverse

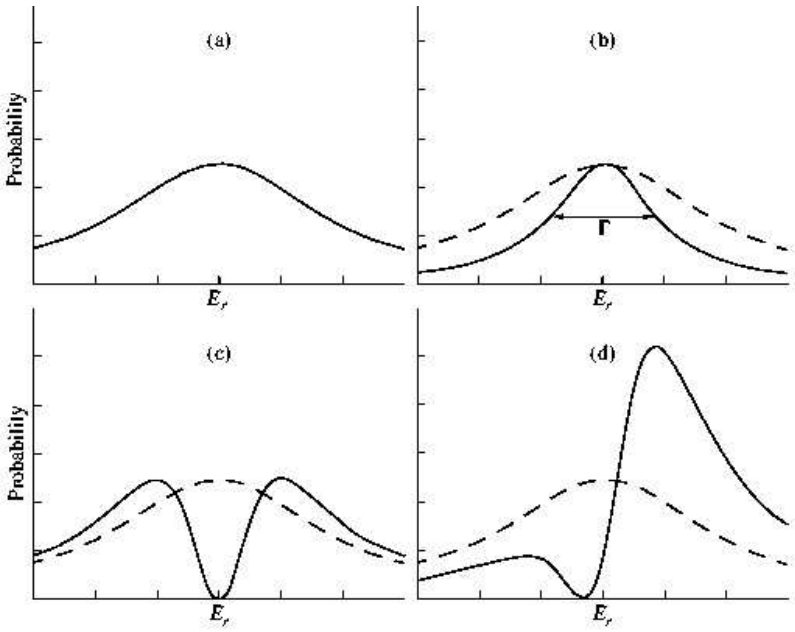

Figure 6.2: Emission spectra P(E) for (a) direct ionization in the absence of the resonance (path 1 in Fig. 5.1), (b) indirect ionization via the resonance with the direct channel blocked ($q = \infty$, path 2 in Fig. 5.1), (c) direct ionization in the presence of a resonance with the resonant channel blocked ($q = 0$, path 1 plus 3 in Fig. 5.1) (curve (a) shown for comparison as dashed line), and (d) Fano profile when both paths are open for $q = 1$.

temporal pulse width of the XUV pulse. By contrast, the width in Fig. 6.2b, representing the indirect ionization via the resonance, is determined by the inverse lifetime of the resonance Γ. This case corresponds to the Auger decay. New features appear when coherences are taken into account. If we consider direct ionization exclusively to the continuum while the transition ($|g\rangle \to |r\rangle$) is blocked (corresponding to $q = 0$) configuration mixing between $|E\rangle$ and $|r\rangle$ (first two terms in Eq. (5.12)) leads to drastic modification of the spectrum with a hole at the resonance energy E_r ("window resonance"), Fig. 6.2c. Finally, when both pathways to the continuum $|g\rangle \to |r\rangle$ and $|g\rangle \to |E\rangle$ are open a typical asymmetric Fano profile emerges, Fig. 6.2d.

The temporal evolution of the autoionization probability $P(E, t)$ is dis-

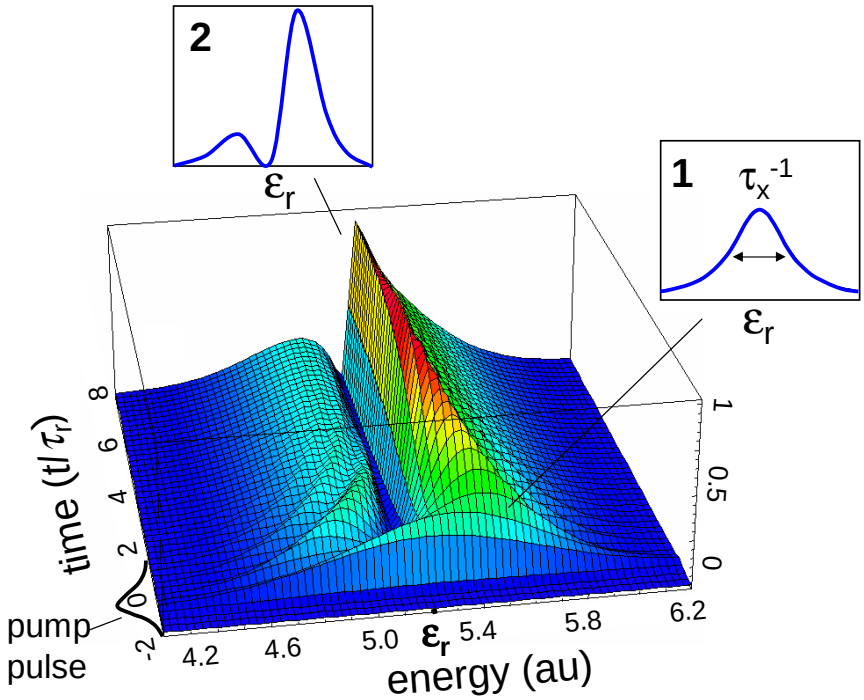

Figure 6.3: Time-dependent ionization probability $P(E,t)$ as a function of energy and time. Inset 1: spectral distribution at short times $t \leq \tau_r$, inset 2: spectral distribution in the limit $t \to \infty$ for $q = 1$.

played in Fig. 6.3 for the typical case of an asymmetric Fano profile in the absence of the probe laser pulse ($q = 1$). In view of anticipated experimental investigations of Super Coster Kronig transitions in the $4d$ giant resonances of the lanthanides (Dzionk et al. [76]), we chose a lifetime of the autoionizing resonance $\tau_r = (2\pi|V_E|^2)^{-1} = 400$ as, an XUV pulse of duration $\tau_X \approx 250$ as and excitation energy of $\hbar\omega_X = 150$ eV. For $t \leq \tau_r$ the broad spectral distribution reflects the width of the XUV pump pulse $\approx \tau_X^{-1}$ (inset 1). For $t \geq \tau_r$ the wave packet representing this spectral distribution acquires an internal structure due to the coupling to the quasi-bound level $|r\rangle$. As a result, the destructive interference due to the transient coupling to the resonance starts to "burn a hole" into the energy distribution at times $t/\tau_r \geq 1$. Finally, in the limit $t \to \infty$ the spectral distribution converges to that of an asymmetric

Fano resonance (inset 2).

For a better understanding of Fig. 6.3 we present the time-dependent ionization amplitude for the case that the exciting pulse is a delta-kick:

$$E_X(t) = E\delta(t). \tag{6.6}$$

In this case an analytic expression can be found for the time-dependent ionization amplitude:

$$\begin{aligned} b_E(t) &= e^{-iEt}a_E + a_R\frac{V_E}{2}e^{-iEt}\frac{e^{-i(E_r-E-i\Gamma/2)t}-1}{E_r-E-i\frac{\Gamma}{2}} \\ &- \frac{i\Gamma}{2V_E}e^{-iEt}\frac{e^{-i(E_r-E-i\Gamma/2)t}-1}{E_r-E-i\frac{\Gamma}{2}}, \end{aligned} \tag{6.7}$$

where a_E and a_R are the excitation matrix elements from the ground state to the continuum $|E\rangle$ and the resonant state $|r\rangle$, respectively. To obtain the time-dependent ionization probability, we have to evaluate $|b_E(t)|^2$. In order to get a more transparent expression we perform the calculation for the case of a window resonance ($q = 0$) i.e. we set $a_r = 0$. Then we obtain:

$$|b_E(t)|^2 = \frac{(E_r-E-\frac{\Gamma}{2}e^{-\Gamma t/2}\sin((E_r-E)t)^2 + \frac{\Gamma^2}{4}e^{-\Gamma t}\cos((E_r-E)t)^2}{(E-E_r)^2+\frac{\Gamma^2}{4}} \tag{6.8}$$

For $t \to \infty$ the expression (6.8) simplifies to

$$|b_E(t)|^2 = \frac{(E_r-E)^2}{(E_r-E)^2+\frac{\Gamma^2}{4}}, \tag{6.9}$$

which is the Fano profile for $q = 0$. Thus for large times t the Fano line shape equals the well known profile. However, what happens for finite times t ? From equation (6.8) we see that terms with $\cos((E_r-E)t)$ and $\sin((E_r-E)t)$ exist. These terms are responsible for the small oscillations which are visible in Fig. 6.3 on each side of the resonance. The amplitude of these oscillations decreases exponentially at least as $e^{-\Gamma/2t}$ so that they are not visible anymore in the asymptotic spectrum.

While we have studied in this chapter the time-evolution of an autoionizing decay initiated by an attosecond laser pulse, we will add the probe laser pulse in the next chapter.

Chapter 7

Simulation of a Pump-Probe Experiment

The atomic rearrangement process described in the previous chapter happens on a sub-femtosecond time scale and is therefore not possible to observe directly in real time. However, pump-probe experiments provide the key to retrieve real-time information about such fast processes by correlating the ionized electron wave packet with a probing light field. Time-resolved spectroscopy based upon this pump-probe approach is now routinely used for tracking atomic motion in molecules with femtosecond laser pulses (Dantus et al. [78]). The time resolution suffices to map out the vibronic motion of molecules (Dantus et al. [78]), the phonon dynamics in solids (Hase et al. [79]), and the electronic dynamics in Rydberg states (Yeazell and C. R. Stroud [80], Raman et al. [81]). Resolving the dynamics of electrons in atoms near the ground states or in inner shells has remained, however, a major challenge. Only very recently, XUV pulses with durations of a few hundred attoseconds have become available (Hentschel et al. [9]). The time structure is comparable to the time scale of electronic processes in inner shells of atoms and opens up the perspective to perform time-resolved measurements of the electronic dynamics in atoms (Nicolaides et al. [82], Mercouris et al. [83]). In a first proof of principle experiment, a 900 as XUV pulse was used to induce a non-resonant core hole excitation in Krypton which relaxes by Auger decay. Its lifetime of about 8 fs was measured in the time domain by probing the "arrival time" of the Auger electron in the continuum with

the envelope of a synchronized fs laser probe-pulse and was found to be in accord with the spectroscopic data (Drescher et al. [11]). More recently, the time evolution of primary electron emission could be measured with a resolution of 100 as by using the controlled oscillation of the electric field of few-cycle probe laser light (Kienberger et al. [84]). The technique has been dubbed attosecond streak camera (Itatani et al. [74]).

In this chapter we study how more complex coherent dynamics proceeding on a time scale comparable to that of the duration of the sub-fs XUV excitation can be probed by this novel technique and to what extent novel information may be obtained from such time-domain studies as compared to conventional time-integral measurements.

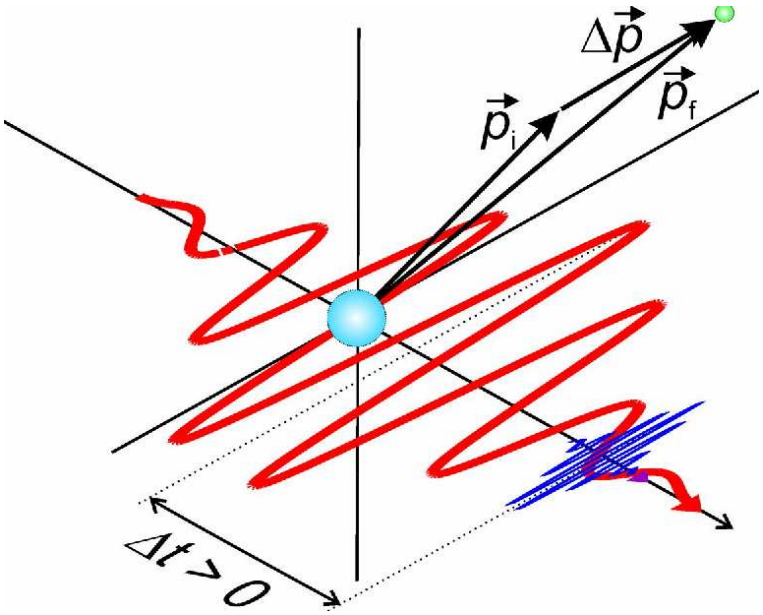

Figure 7.1: Schematic picture of the two color sampling technique for probing electron emission from atoms. The XUV-pulse excites and/or ionizes the atomic target. The delayed probe pulse transfers a momentum shift $\Delta\mathbf{p}$ to the ejected electron after its release. The transfered momentum sensitively depends on the phase and amplitude of the probe laser light at the instant of release of the electron. This results in a time-to-energy mapping on an attosecond time scale. (Figure taken from (Drescher et al. [11]))

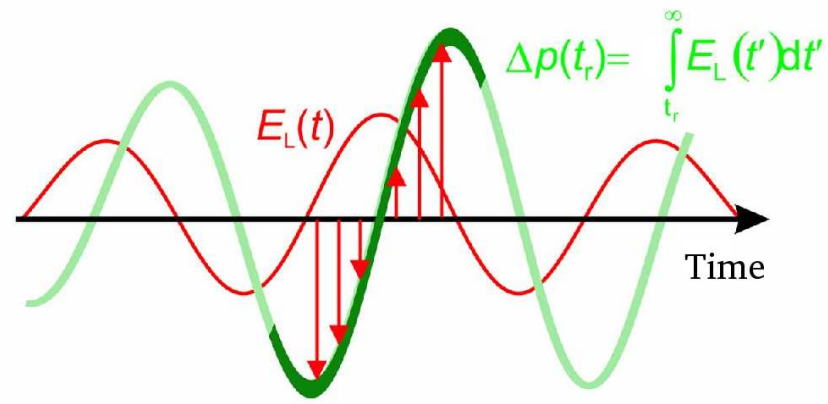

Figure 7.2: Schematic illustration of the laser phase dependence of the momentum transfered to the emitted electron by the probe laser pulse. For ionization at the maximum field strength the momentum shift Δp is zero, whereas ionization near the minimum field strength leads to a maximum momentum shift.

Fig. 7.1 is a schematic illustration of the pump-probe technique. The pump pulse excites or ionizes an electron which then moves in the combined field of the laser and the XUV-pulse. The red and blue curves represent the evolutions of the electric field of the laser and the XUV-pulse, respectively. Both pulses are focused simultaneously into the gas target with a well controlled delay time Δt. The XUV pulse excites the atom which then emits an electron. The electrons ejected in the polarization direction of the laser are detected. They undergo, depending on the time of their emission a change of momentum Δp, as seen in Fig. 7.1. The total momentum and thus the momentum shift is finally measured with a time-of-flight spectrometer. The momentum shift of the ionized electrons due to the laser pulse is given by:

$$\Delta p = \int_{t_i}^{\infty} E_L(t')dt' = \tilde{A}(t_i), \tag{7.1}$$

where t_i is the time of ionization. Obviously, the momentum shift Δp is proportional to the vector potential at the time of ionization.

Two limiting cases can be distinguished. For ionization processes lasting less than the light field cycles $\tau_r \ll T_L$, the oscillating light field constitutes a sub-femtosecond probe. The energy spectrum fluctuates due to the oscilla-

tions of the vector potential $\tilde{\mathbf{A}}(t)$ entering the canonical momentum and thus resembles the behavior of a classical particle in an oscillating electric field. In the opposite limit of long lifetime compared to the period of the probe pulse, $\tau_r \gg T_L$, the quantized nature of the interaction of the electron with the radiation field is retained and energy shifts occur in multiples of the photon energy $\hbar\omega_L$ giving rise to spectral sidebands. These processes are sampled by the amplitude envelope of the laser pulse. In both cases a sequence of light-affected electron spectra are recorded at different delays Δt, from which the time evolution of electron emission can be reconstructed. The resulting signal depends on three different time scales: the lifetime of the resonance, τ_r, the duration of the pump pulse, τ_X, and the period, T_L, of the probe pulse.

7.1 Pump-probe spectra for photoionization

The intensity which we have used for the probe laser pulse is 5×10^{11} W/cm^2, which is small enough so that ionization by the probe laser pulse can be neglected. Additionally, the intensity of the pump pulse is about three orders of magnitude smaller than the intensity of the probe laser so that the pump-pulse $F_X(t) = F_X\cos(\Omega t)f_X(t)$ does not influence the motion of the ionized electron. We assume both envelope functions f_X and f_L to be Gaussians where the duration of the probe pulse is long compared to that of the pump $\tau_L \gg \tau_X$ (in current experiments $\tau_L \geq 5$ fs). These are typical experimental parameters as have been used e.g. in (Goulielmakis et al. [10], Drescher et al. [11]).

In the following we present results for two different lifetimes of the resonant state, $\tau_r = 250$ as and for comparison, a significantly larger lifetime of $\tau_r = 2.5$ fs. A rich variety of spectral features as a function of pump-probe delay time can be observed. The key point is that these intricate features in $P_{\Delta t}(E)$ appear only when all three time scales τ_X, τ_r and T_L are comparable to each other.

Fig. 7.3 shows the simulated spectra as a function of pump-probe delay for the case of photoionization in the absence of the resonance. For a constant delay time the spectral line shape is a Gaussian due to the Gaussian envelope of the ionizing pulse. It is visible from Fig. 7.3 that the center of the line

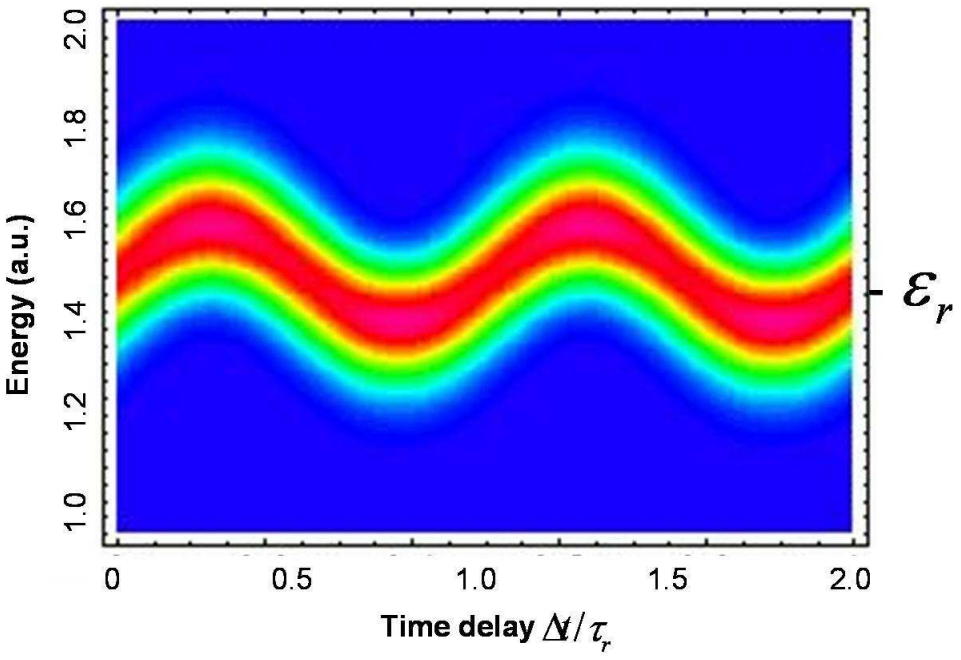

Figure 7.3: Simulated electron spectra for direct ionization as a function of time-delay between pump and probe pulse observed in the direction of the polarization direction of the probe laser pulse. The spectra follow the oscillations of the probe laser pulse. We use a 500 as XUV-pulse with a photon energy of 100 eV and a 10 fs (FWHM) probe pulse with a period of 2.5 fs and a photon energy of 1.55 eV.

shape follows the oscillations of the probe laser pulse. For this simulation we have used a 500 as XUV-pulse with a photon energy of 100 eV and a 10 fs (FWHM) probe pulse with a cycle period of 2.5 fs which corresponds to a photon energy of 1.55 eV.

7.2 Pump-probe spectra for a single resonance

In Fig. 7.4 the pump-probe spectra for (a) an Auger-decay and (b) for an autoionizing decay with a Fano parameter of $q = 0.5$ are presented. We note that the case of the time-resolved Auger decay, which has been experimentally realized (Drescher et al. [11]), has already been theoretically investigated. In

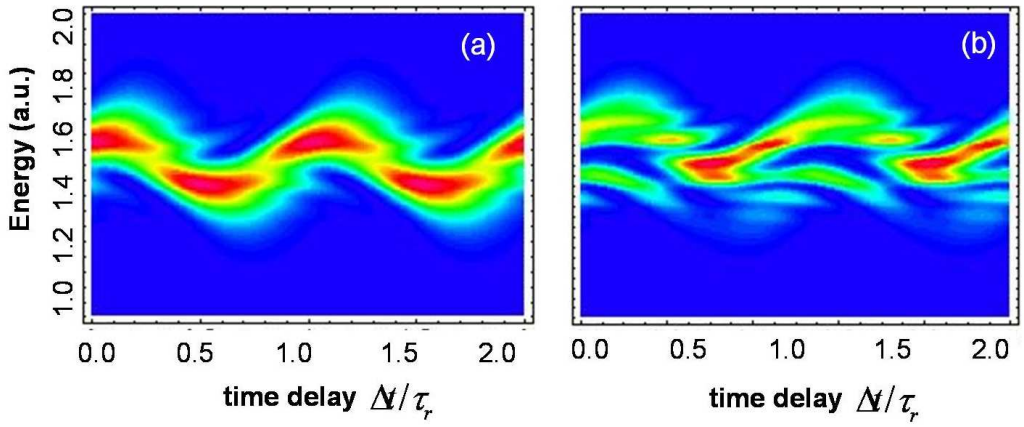

Figure 7.4: Simulated electron spectra for (a) resonant ionization (Auger decay) and (b) excitation of a Fano resonance with $q = 0.5$ as a function of time-delay between pump and probe pulse observed in the direction of the polarization direction of the probe laser pulse. The lifetime of the resonant state was chosen to be 250 as. The spectra follow the oscillations of the probe laser pulse. We use a 500 as XUV-pulse with a photon energy of 100 eV and a 10 fs (FWHM) probe pulse with a period of 2.5 fs and a photon energy of 1.55 eV.

(Drescher et al. [11], Smirnova et al. [12]) the transitions from a quasi-classical energy shift of the spectrum to the formation of sidebands was explained. The lifetime of the resonance was chosen to be 250 as. Since the lifetime of the resonance is so short, the spectra look similar to the case of photoionization without a resonance present. Fig. 7.4b looks more complicated because of the two interfering pathways, however, the asymmetric Fano profile is still recognizable.

In Figs. 7.5(a,b) we present the pump-probe spectra for the same parameters as in Figs. 7.4(a,b), however we chose a lifetime of 2.5 fs for the resonance. Fig. 7.5a shows the well-known sidebands spaced by the photon energy. The first and second order sideband which correspond to the absorption of one and two photons, respectively, are visible in the figure. In Fig. 7.5b the sideband structure is still visible, however on top of this struc-

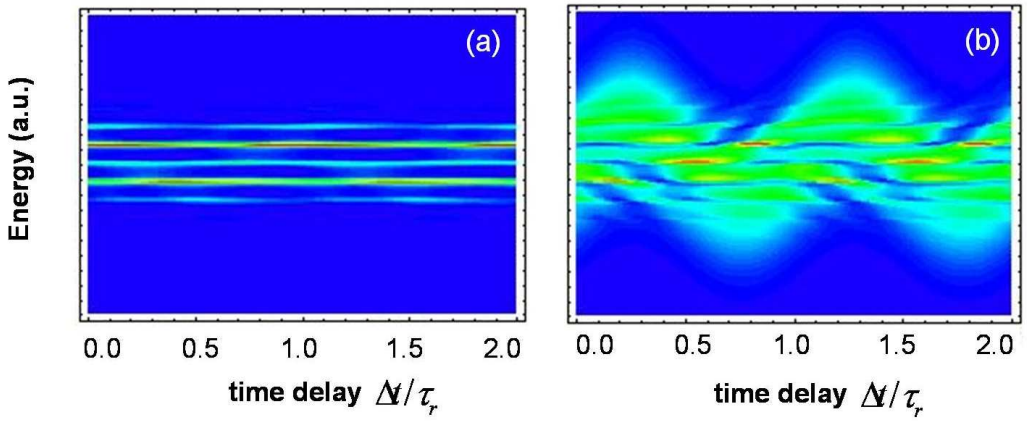

Figure 7.5: Simulated electron spectra for (a) resonant ionization (Auger decay) and (b) excitation of a Fano resonance with $q = 0.5$ as a function of time-delay between pump and probe pulse observed in the direction of the polarization direction of the probe laser pulse. The lifetime of the resonant state was chosen to be 2.5 fs. The spectra follow the oscillations of the probe laser pulse. We use a 500 as XUV-pulse with a photon energy of 100 eV and a 10 fs (FWHM) probe pulse with a period of 2.5 fs and a photon energy of 1.55 eV.

ture an oscillatory behavior can be see. These oscillations are caused by the direct ionization channel. The population of the sidebands is caused by the resonant channel. Thus, time-resolved spectroscopy allows to separate the two interfering ionization channels because of their different temporal behavior.

7.3 Breaking of time-reversal symmetry: Complex Fano parameter

One extension of this approach is the investigation of a complex Fano parameters. In the original work of Fano (Fano [22]) and most subsequent studies based on this theory, the asymmetric parameter q has been implicitly treated

as a real number. However, this is only valid when the system has the time-reversal symmetry, and thus the matrix elements defining q can be taken as real. A system is said to exhibit symmetry under time reversal if, at least in principle, its time-evolution may be reversed and all physical processes run backwards, with initial and final states interchanged. In (Kobayashi et al. [85, 86], Clerk et al. [87]) it was reported that in the presence of a magnetic field or decoherence, both which break the time-reversal symmetry, a complex Fano parameter could be observed. In these experiments the Fano line shape was observed in the conductance of a quantum dot where the interference of direct and resonant trajectories connecting source and drain lead to the typical Fano profile. The specific Fano line shape is thus sensitive to the phase coherence between the resonant and the non resonant pathways. The magnetic field systematically affects the phase difference between the two paths so that a complex Fano parameter can be tuned. The decoherence, which can be e.g. controlled by the increase of temperature, leads to a loss of phase information between the interfering pathways, so that the contribution from the different pathways add up incoherently which gradually leads to a symmetric line shape. In case of an atom in a laser field there is no magnetic field and also decoherence with respect to collisions with other gas atoms is assumed to be negligible. However, the laser probe field itself influences the ionization process and can cause depopulation of the resonant state. This system has to be treated now like an open quantum system which can be described with an effective complex Fano parameter. The resonant state is assumed to be only weakly perturbed by the probe laser field which can be taken into account by a complex dynamical Stark shift $\Delta E_S^c(t)$ that includes both a real energy shift ΔE_S as well as a damping due to coupling to other states outside the subspace of the Fano resonance. However, we will not include the Stark shift directly into our formalism but discuss only the issue of an effective complex Fano parameter.

The line shape for a resonance with a complex Fano parameter q can be parameterized near the resonance energy by the same simple formula as (6.1),

$$P(\epsilon) = \frac{|q+\epsilon|^2}{1+\epsilon^2} \tag{7.2}$$

with

$$\epsilon = \frac{E - E_r - \delta E}{\Gamma/2}. \tag{7.3}$$

The issue of a complex Fano parameter is of special interest to us, since we have found that time-resolved measurements are extremely phase sensitive and can provide us with more information than conventional time-integral measurements. One remarkable feature of the time-integral spectral distribution $P(E)$ is that it is invariant under complex conjugation $q \to q^*$ as seen from equation (7.2), i.e. the phase angle of the Fano parameter cannot be uniquely determined. The time-resolved spectrum, instead, $P_{\Delta t}(E)$, is found to be sensitive to this phase angle.

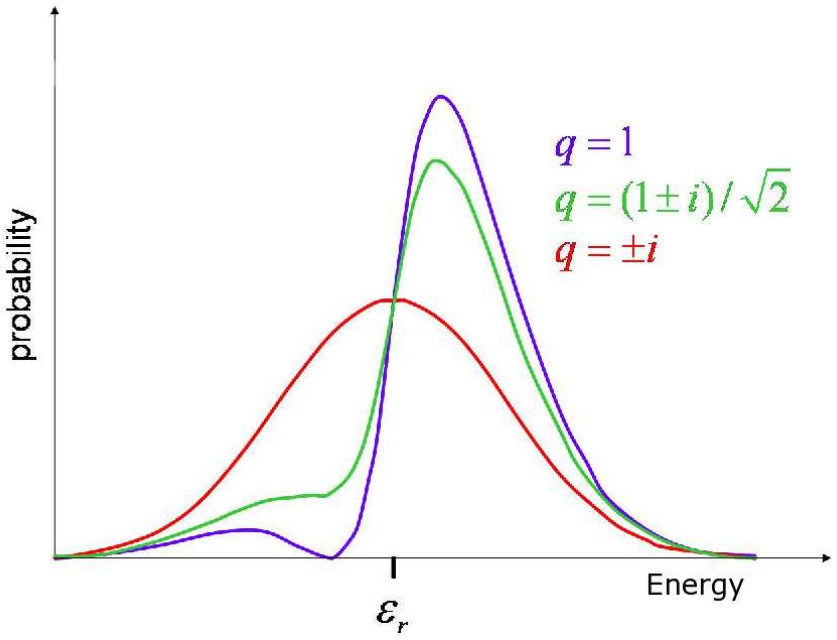

Figure 7.6: Fano profiles for complex Fano parameters, $q = 1$, $(1 \pm i)/\sqrt{2}$ and $\pm i$, respectively. All five q-parameters satisfy $|q|^2 = 1$. With increasing imaginary part the spectra become more symmetric. The spectral line shape is identical for q and the complex conjugate Fano parameter q^*.

Fig. 7.6 shows the line shapes for different complex Fano parameters. All q parameters in this figure fulfill $|q|^2 = 1$. They only differ in a complex phase. Obviously, with increasing imaginary part of the Fano parameter, the

profiles become more symmetric. For $q = \pm i$ a totally symmetric line shape is observed. As is visible in Fig. 7.6, the spectral line shapes are identical for q and the complex conjugate Fano parameter q^*.
This motivated us to study this symmetry in more detail. In Fig. 7.7 we compare the time evolution of the ionization probability for the two Fano parameters $q = \pm i$. Although, asymptotically both q parameters lead to the same line shape, as is visible in Fig. 7.7, the time-evolution differs. In the case of $q = i$ the time-evolution of the ionization signal exhibits a very smooth pattern compared to the case of $q = -i$ where several interference structures can be seen in the figure.

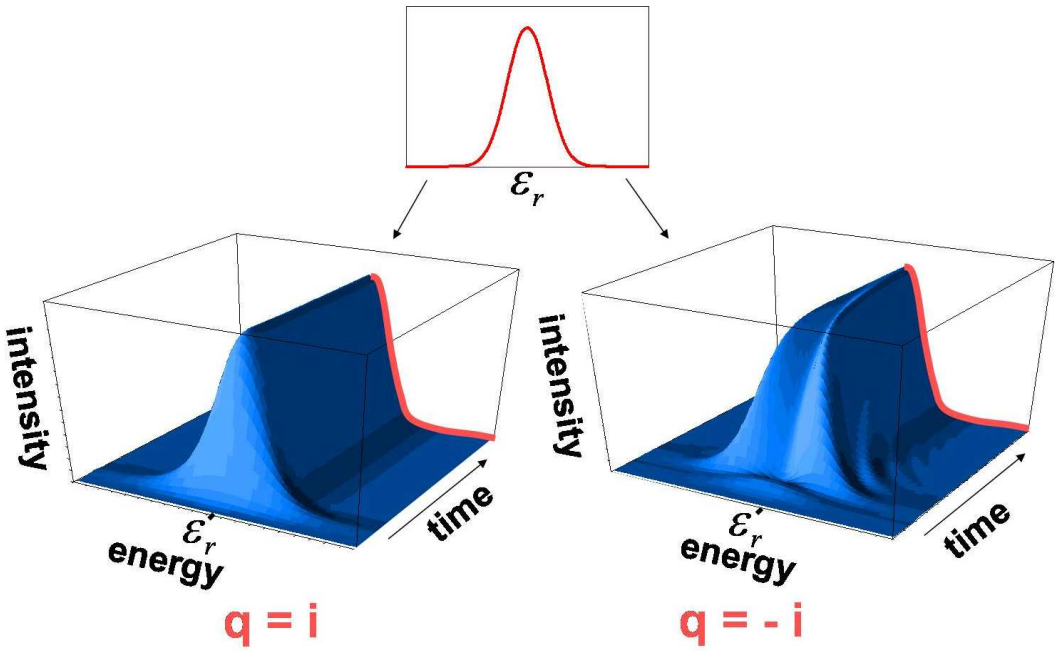

Figure 7.7: Time dependent ionization probability for $q = \pm i$. The asymptotic spectrum is shown in the middle. Although the asymptotic spectrum is identical for both Fano parameters the time dependent ionization probability differs.

In equation (5.12) it was shown that the total ionization amplitude for an autoionizing decay can be split up into three parts: First, the direct

ionization amplitude in the absence of the resonance, second, the correction to the direct ionization channel due to coupling with the resonant state and third, the resonant ionization amplitude. We use the following notation for the different ionization amplitudes:

$$A_{\text{total}} = A_{\text{direct}} + A_{\text{correction}} + A_{\text{resonant}} \tag{7.4}$$

With the help of the relation

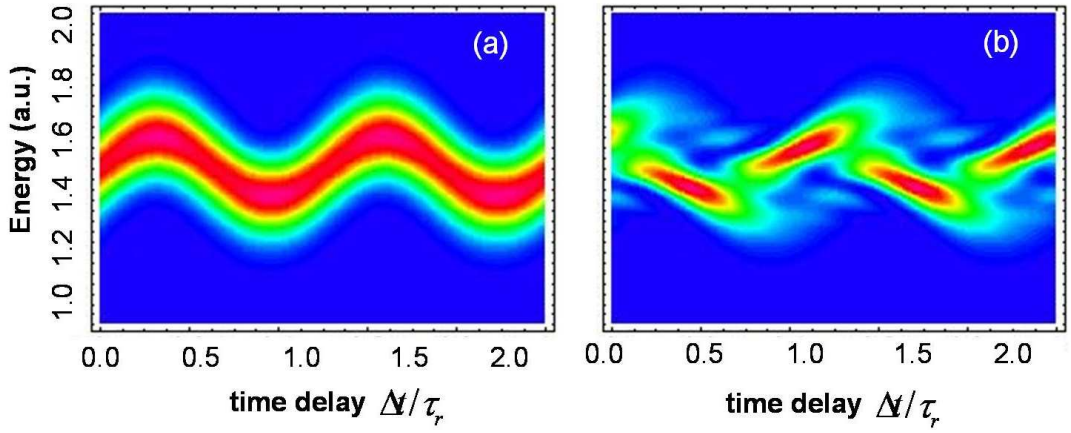

Figure 7.8: Simulated pump-probe spectra for (a) $q = i$ and for (b) $q = -i$. The spectral line shapes of these two Fano parameters are identical, however the pump probe spectra reflect the different time-dependent ionization probabilities and thus clearly differ.

$$\langle r|U_F(t'',t')|E\rangle = \frac{\sin(\Delta(E)}{\pi V_E} e^{i\Delta(E)} \left(e^{-i(E_r - i\Gamma/2)(t''-t')} - e^{-iE(t''-t')}\right) \tag{7.5}$$

the energy integral in equation (5.12) can be solved analytically. Under the assumption that the matrix elements V_E and $\langle E|z|g\rangle$ are energy independent, which is near the resonant energy a reasonable approximation, and the relation

$$\int dE\langle r|U_F(t,t')|E\rangle a_E(t') = -ie^{-\frac{\Gamma}{2}(t-t')-iEr(t-t')}a_{Er}(t')\pi V_E r, \tag{7.6}$$

it follows from equation (5.12) that

$$A_{\text{resonant}} = iqA_{\text{correction}} \tag{7.7}$$

From equation (7.7) we see now that the total ionization amplitude for the case of a Fano parameter of $q = i$ simplifies to

$$A_{\text{total}} = A_{\text{direct}} \tag{7.8}$$

and in the case of $q = -i$ the total ionization amplitude equals

$$A_{\text{total}} = A_{\text{direct}} + 2A_{\text{resonant}}. \tag{7.9}$$

Asymptotically, both spectra are identical, but from the equations (7.9) and (7.8) it can be seen that the ionization amplitudes are not the same. For the case of $q = -i$ the ionization amplitude contains the resonant ionization channel. The time structure of this channel is dominated by the mean life time of the resonant state. On the contrary, the ionization amplitude for the case of $q = i$ is identical to the direct ionization in the absence of the resonant state and therefore the time structure of this channel is only influenced by the duration of the pump-pulse. Thus is it possible to distinguish these two Fano parameters with the pump-probe technique.

In Fig. 7.7 we present the simulated pump-probe spectra for $q = \pm i$. The spectra reflect the different time-dependent ionization probabilities and therefore clearly differ. Fig. 7.7a shows the case for $q = i$. As seen from equation (7.8) the amplitudes interacting with the resonant state destructively interfere and only the direct ionization channel remains. This figure is therefore identical to Fig. 7.3. In Fig. 7.7b the resonant character of the ionization amplitude with the longer lifetime of 500 as becomes visible. Although only for the special case of $q = \pm i$ total destructive or constructive interference occurs, it is in general possible to distinguish the two Fano parameters q and $q*$ from the pump-probe spectra.

In this chapter we have presented simulated spectra for a pump-probe experiment for the case of an autoionizing state. We have shown that the

different ionization channels, the direct and the resonant one, can be distinguished in a pump-probe experiment because of their different time-structure. In the last section we have shown that in the case of a complex Fano parameter, time-resolved spectroscopy is able to provide more information than conventional time-integral measurements.

Chapter 8

Excitation of Two Nearby Resonances

A future goal for time-resolved studies will be to probe and control the electron dynamics in a many-electron system which cannot be fully resolved by conventional spectroscopy. The analysis in the previous chapter was restricted to a single isolated resonance. In view of the broad spectral width of the attosecond XUV pulse, excitation of an isolated resonance will be the exception rather than the rule. Instead, several near-by Fano resonances will be simultaneously and coherently excited. Coherent excitation of several resonances by an ultrashort pulse has been studied e.g. in (Zhao and Lin [68]). Additionally, similar excitation processes in ion-atom collisions have been investigated quite some time ago (von den Straten and Morgenstern [88]). The post-collision interaction (PCI) energy shift was, in fact, used as an effective "streaking" technique. The excitation of a collective dipole oscillation and vibronic motion of the two-electron doubly excited states in He could be mapped out (Burgdorfer and Morgenstern [73], von den Straten and Morgenstern [88]).

In this chapter, which is a more complete version of (Wickenhauser et al. [30]) we will discuss the attosecond streaking for coherent excitation of closely spaced resonances. We focus for simplicity on two nearby resonances. A central issue to be addressed is the information that possibly can be extracted from such more complex streaking images. In principle, information on both

the atomic structure parameters (position and width of the resonances), and the excitation amplitudes or, more generally, the excitation density matrix should become available. In view of the rich and complicated structure of streaking images, one can only expect in simple cases to completely disentangle and extract this information.

8.1 Line Shapes and Energies

The atomic model system that we consider in this chapter consists of a ground state $|g\rangle$ and two resonant states $|a\rangle$ and $|b\rangle$ embedded in a structureless continuum $|E\rangle$ (Fig. 8.1).

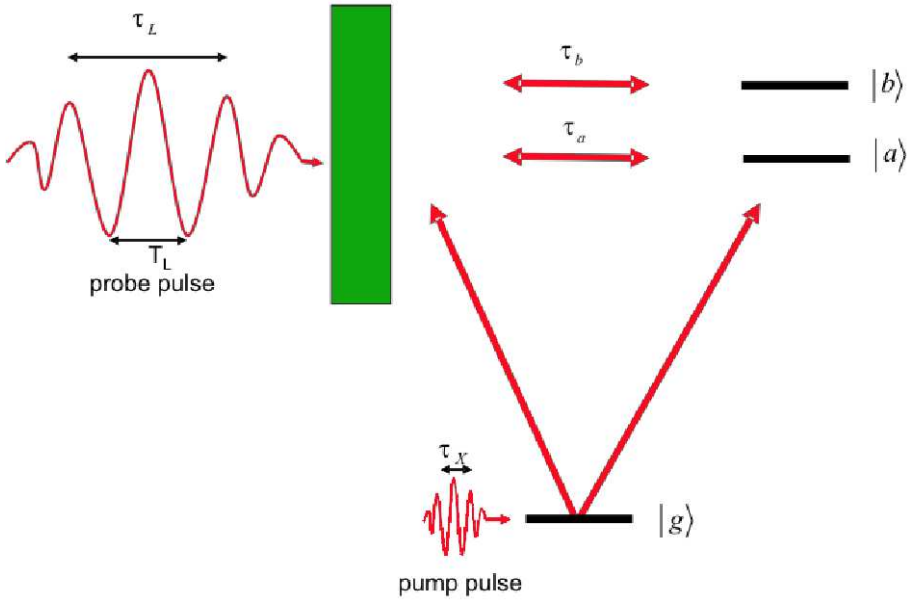

Figure 8.1: Schematic picture of the autoionization process for two nearby resonances. The ultrashort pump pulse coherently excites both resonances which are assumed to be in the same angular momentum sector. Additionally, photoelectrons can be directly ionized by the XUV-pulse which leads to three interfering paths from the ground state to the one-electron continuum. Arrival in the continuum is monitored by the probe laser pulse with period $T_L = 2\pi/\omega_L$ and length τ_L.

The resonant states lie above the ionization threshold of the field-free

Hamiltonian. We study the time evolution of this system under the influence of a sub-fs high-frequency low-intensity pump pulse which initializes the autoionization process and a low-frequency, moderate-intensity probe pulse. The Hamiltonian

$$H(t) = H_0 + V + H_X(t) + H_L(t) \tag{8.1}$$

consists of the atomic Hamiltonian $H_a = H_0 + V_a + V_b$, where H_0 is the single configuration Hamiltonian and $V_k (k = a, b)$

$$V_k = \int dE |E\rangle V_{Ek} \langle k| + h.c. \tag{8.2}$$

describe the interaction between the resonances and the continuum. All dependences on angular momentum and emission angles are suppressed and the emission direction is assumed to be along the direction of the polarization of the laser field. In the absence of the coupling between the resonant states and continuum, $|a\rangle$ and $|b\rangle$ would be bound eigenstates of H_0.

The simple expression from the previous chapter (Equation (6.1)) to parameterize a resonance becomes more complicated in the presence of a second resonance. Interferences cause a much more complex behavior. The time-independent approach of this problem is well understood (Fano [22], Magunov and Strakhova [89]). Time-resolved studies provide however an alternative approach. They can, for example, facilitate the disentangling of overlapping resonances that cannot be resolved spectroscopically.

We will analyze first streaking images of two overlapping Lorentz resonances. Related problems have been studied in detail in many different subfields, among others for dressed states in laser fields (Coleman and Knight [90], Coleman et al. [91]) and in quantum chaos, to name just a few. Lorentz resonances correspond to the limit that the direct pathway to the continuum is blocked (see Fig. 8.1), i.e. the direct ionization channel is absent or equivalently, that $|q_a|, |q_b| \to \infty$. In the limit of two separated resonances each resonance is characterized by an energy position and a width. However, if the energy spacing between the two resonances becomes comparable to the width, the two resonances interact via the continuum and the energy positions E_k and widths Γ_k change according to (see, e.g., (Magunov and

Strakhova [89], Coleman and Knight [90], Coleman et al. [91]))

$$\begin{aligned} \tilde{E}_k - i\frac{\tilde{\Gamma}_k}{2} &= \frac{E_a + E_b}{2} - i\left(\frac{\Gamma_a}{4} + \frac{\Gamma_b}{4}\right) \pm \\ &\pm \left(\frac{(E_a - E_b)^2}{4} - \frac{(\Gamma_a + \Gamma_b)^2}{4} \mp \frac{i}{4}(E_a - E_b)(\Gamma_a - \Gamma_b)\right)^{1/2} \end{aligned} \tag{8.3}$$

with $\Gamma_k = 2\pi\,|V_k|^2$.

The coupling of two resonances leads to "avoided crossings" in the complex energy plane (Magunov and Strakhova [89], Yang et al. [92]). In the special case that the direct coupling between resonances is suppressed and only indirect coupling via the continuum is present, the coupling results in level attraction along the real axis and repulsion along the imaginary axis (splitting of the widths). The latter leads to a pair of long-lived and short-lived resonances which can even lead to a bound state (with infinite lifetime) in the continuum. The appearance of two disparate time scales may be directly observable in the time-resolved emission. For example two near-by resonances with spacing $\Delta E = E_a - E_b$ and identical width $\Gamma_a = \Gamma_b = \Gamma$ in the absence of continuum coupling. Introducing the parameter $\kappa = \Delta E/\Gamma$, Eq. (8.3) can be rewritten as

$$\tilde{E}_k - i\frac{\tilde{\Gamma}_k}{2} = \frac{E_a + E_b}{2} - i\frac{\Gamma}{2} \pm \frac{1}{2\Gamma}(\kappa^2 - 1)^{1/2}\,. \tag{8.4}$$

For $\kappa > 1$, corresponding to the case of two weakly interacting resonances, both resonances have still the same lifetime, but are located at different energies. For $\kappa < 1$ different time scales appear. One resonance becomes long lived while the other one becomes short lived. This corresponds to a repulsion on the imaginary axis accompanied by attraction of the levels on the real axis.

Fig. 8.2 shows the time-integral spectra for two Lorentz resonances with width $\Gamma_a = \Gamma_b = 0.05$. The energy spacing ΔE is four, two and 0.2 times the width of the resonances in Figs. 8.2 (a), (b) and (c), respectively. As long as the energy spacing is larger than the width both resonances have still the same width (in the case of $\Gamma_a = \Gamma_b$) and are located at different energies. As the control parameter κ falls below unity, i.e. the width becomes larger than the spacing between the two resonances, the resulting energy positions $\tilde{E}_\kappa$ become equal while the lifetimes split into one long-lived and one

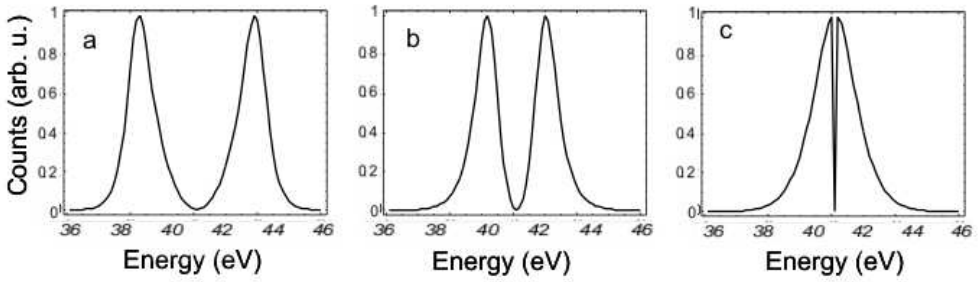

Figure 8.2: Spectra for two Lorentz resonances with half widths $\Gamma_a = \Gamma_b = 0.05$. The parameter κ is 4, 2 and 0.2 in (a), (b) and (c), respectively. In (a) and (b) still both resonances have the same width but are located at different energies. By contrast, in (c) two resonances are located at the same energy position but feature different lifetimes.

short-lived resonances. Time-resolved measurements open up the possibility to directly observe the emerging disparate time scale. As will be shown below the method of streaking provides a novel avenue to study time-resolved dynamics of resonances.

8.2 Time-dependent analysis

Our starting point for treating time-dependent autoionization with two resonances coherently excited by an ultrashort pulse is the solution of the time-dependent rather than the stationary Schrödinger equation, i.e.,

$$|\psi(t)\rangle = \hat{T} e^{-i\int_{-\infty}^{t} H(t')dt'} |g\rangle \ , \tag{8.5}$$

where $\hat{T}$ denotes the time-ordering operation (see (5.4)).

The goal is to calculate the time-and energy-differential ionization probability $P(E,t) = |\langle E|\psi(t)\rangle|^2$. We solve Eq. (8.5) under a number of simplifying assumptions (Wickenhauser et al. [25]) similar to the previous chapter. The weak XUV pulse is treated in first-order perturbation theory and we neglect all other couplings except those involving the ground state. Additionally, the action of the probe laser on the ground state is neglected.

Thus the propagator of Fano states (compare 5.6) takes on the form

$$U_F(t,t') = \hat{T}\ \exp[-i\int_{t'}^{t} dt''(H_0 + V_a + V_b)]. \tag{8.6}$$

With these approximations, the time-energy differential ionization amplitude becomes

$$\begin{aligned}
\langle E|\psi(t)\rangle &= -i\int_{-\infty}^{t} dt' e^{i\Phi_V(E,t',t)}\dot{a}_{E(t',t)}(t') \qquad (8.7)\\
&-\int_{-\infty}^{t} dt'\int_{t'}^{t} dt''\int d\tilde{E} e^{i\Phi_V(E,t'',t)}(V_{E(t'',t)a}\langle a| + V_{E(t'',t)b}\langle b|)U_F(t'',t')|\tilde{E}\rangle\dot{a}_{\tilde{E}}(t')\\
&-\int_{-\infty}^{t} dt' \int_{t'}^{t} dt'' e^{i\Phi_V(E,t'',t)}(V_{E(t'',t)a}\langle a| + V_{E(t'',t)b}\langle b|)U_F(t'',t')|a\rangle\dot{a}_a(t')\\
&-\int_{-\infty}^{t} dt' \int_{t'}^{t} dt'' e^{i\Phi_V(E,t'',t)}(V_{E(t'',t)a}\langle a| + V_{E(t'',t)b}\langle b|)U_F(t'',t')|b\rangle\dot{a}_b(t')
\end{aligned}$$

with $\dot{a}_E(t) = \langle E|H_X(t)|g\rangle_t$ and $\dot{a}_k(t) = \langle k|H_X(t)|g\rangle_t$. Here and in the following is the time derivative of a function denoted by a dot. Under the assumption of energy-independent matrix elements for the configuration interaction $V_{Ea} = V_a$, $V_{Eb} = V_b$ and the direct dipole coupling to the continuum $\langle E|d|g\rangle = \langle c|d|g\rangle$, the integration over energy in Eq. (8.7) can be performed analytically leading to time-energy differential ionization amplitude:

$$\begin{aligned}
\langle E|\psi(t)\rangle &= -\int_{-\infty}^{t} dt' e^{i\Phi_V(E,t',t)} \times \qquad (8.8)\\
&\times\left(i\dot{a}_{cont}(t') + (1+\frac{i}{q_a})\int_{-\infty}^{t'} dt''\dot{R}_a(t',t'') + (1+\frac{i}{q_b})\int_{-\infty}^{t'} dt''\dot{R}_b(t',t'')\right)
\end{aligned}$$

with

$$q_k = \frac{\langle k|d|g\rangle}{\pi\tilde{V}_k\langle c|d|g\rangle} \tag{8.9}$$

and

$$\dot{R}_k(t',t'') = (\tilde{V}_a\langle a|U_F(t',t'')|k\rangle + \tilde{V}_b\langle b|U_F(t',t'')|k\rangle)\dot{a}_k(t'') \tag{8.10}$$

In Eqs. (8.8) and (8.9) we have neglected small energy shifts due to the off-shell coupling between resonances involving the principal part integrals (see the discussion in Ref. (Fano [22])) in line with the assumption of energy-independent couplings V_k.

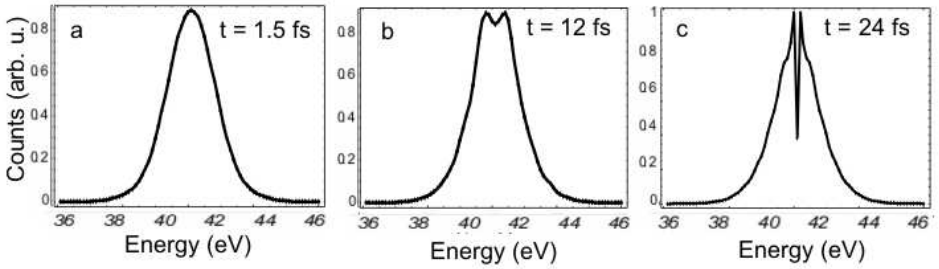

Figure 8.3: Time dependent ionization probability for three different times for the resonance parameters $E_a = 1.495, E_b = 1,505, \Gamma_a = \Gamma_b = 0.05$ corresponding to $\tilde{E}_a = \tilde{E}_b = 1.5$ and $\tilde{\Gamma}_a = 0.05, \tilde{\tau} = 0.4\, fs\ \tilde{\Gamma}_b = 0.0005, \tilde{\tau}_b = 40\, fs$ and $\kappa = 0.2$, and $a_a = a_b$.

The three terms in equation (8.8) represent different coherent pathways to the continuum final state: the first term describe the direct ionization from the ground state to the Volkov continuum in the absence of a resonance. The second and third terms contain a correction to the direct ionization coming from interactions with the resonant states as well as the resonant decay channels. Eq. (8.8) has the apparent structure of two independent Fano resonances. However, each function $\dot{R}_k(t', t'')$ contains the couplings between the two resonances and depends on the parameters of both resonances.

8.3 Pump-probe spectra

As a first example of the resolution in the time domain of the confluence of interacting Lorentz resonances, we present in Fig. 8.3 the time-differential emission spectrum $|\langle E|\psi(t)\rangle|^2$ for the system parameters of Fig. 8.2c. Note that the effect of the probe pulse is not yet included in Fig. 8.3 (see below). After a time of 1.5 fs only the broad resonance corresponding to a lifetime of $\tilde{\tau}_a = 0.4$ fs is visible. The presence of a much longer lived resonance at the same spectrum position ($\tilde{E} = 1.5$ a.u. or 40.8 eV) manifests itself only much later at times of the order of the life time $\tilde{\tau}_b \approx 40$ fs. It results in a pronounced dip by interference between the channels at the common position of the two resonances when the two partial amplitudes have the same sign, $a_a(t) = a_b(t)$ (Fig. 8.3a). In the limit $t \to \infty$ the spectral distribution of Fig. 8.2c is

recovered. Note that the asymptotic spectral distribution resembles that of a single window resonance ($q = 0$) even though in the present case $q_a = q_b \to \infty$. The snapshots at short to intermediate times are, however, different. In particular, the spectral distribution at short times ($\tau < 10$ fs) is independent of the spectral width of the exciting XUV attosecond pulse contrary to the case of a time-resolved window resonance (Wickenhauser et al. [25]) but is Lorentzian with the intrinsic width of the broader of the two resonances.

The destructive interference between the two Lorentz resonances is controlled by the relative phase between the excitation amplitudes $a_k(t)$. More generally, the time-differential ionization probability will depend (in the absence of the direct channel) on the bilinear form

$$\rho_{k,k'} \sim \sum_{k,k'} (1 + i/q_k)\,(1 - i/q_{k'}) \int_{-\infty}^{t} dt'' \int_{-\infty}^{t} dt'\, \dot{R}_k\,(t, t')\, \dot{R}^*_{k'}\,(t, t'')\;, \qquad (8.11)$$

which, is proportional to $\rho_{k,k'} \sim \langle a_k\, a^*_{k'} \rangle$, i.e. the excitation density matrix for the subspace of resonances. Observation of the time-differential ionization probability can, therefore, give access to the elements of the excitation density matrix and thus information of the excitation process, generally not extractable from time-integral measurements.

Fig. 8.4 represents the streaking camera image pertaining to the coalescent Lorentz resonances of Fig. 8.3a. The existence of two resonances with disparate lifetimes manifests itself by the simultaneous presence of the quiver oscillation of the light field and the presence of sidebands. While the former is characteristic for a fast decay process with $\tilde{t}_a < T_L$, the latter is a hallmark of a long-lived state with $\tilde{t}_b \gg T$ which interacts with the light field via photon absorption and emissions.

As a second example we consider the case of well-separated resonances, i.e. where the energy spacing ΔE is much larger than the width of the resonances. We employ a parameter set modeled after the $N = 5$ double-excitation Rydberg series of He (Domke et al. [93]). We choose two window resonances ($q_a = q_b = 0$) at the energies $E_a = 76.32$ eV and $E_b = 76.46$ eV with widths $\Gamma_a = 25.2$ meV and $\Gamma_b = 14.2$ meV corresponding to lifetimes of about 27 fs and 47 fs respectively. A cut through the streaking image along the first sideband at $(E_a + E_b)/2 + \omega_L$ (Fig. 8.5) displays several characteristic features of the coherent excitation of two nearby resonances. The beat frequency is

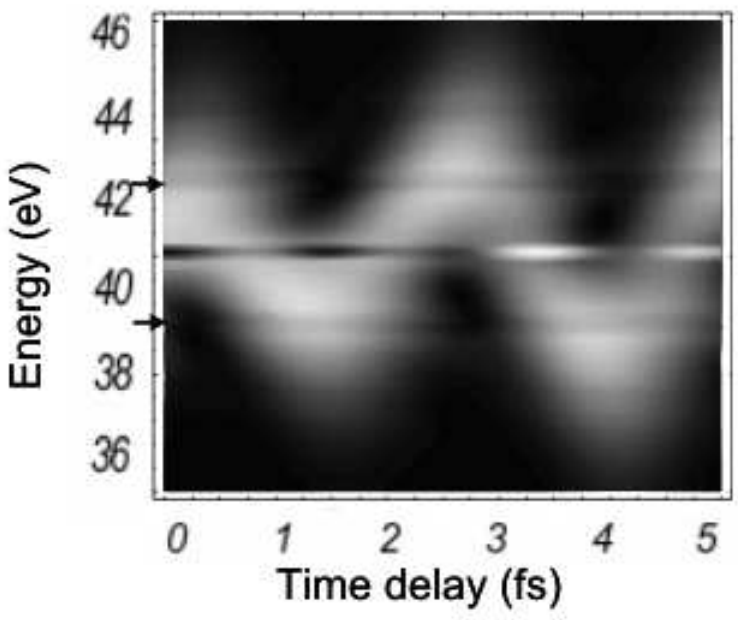

Figure 8.4: Streaking image corresponding to the excitation of two strongly overlapping Lorentz resonances as a function of the time delay between pump and probe pulse observed in the polarization direction of the probe laser pulse. The arrows indicate the positions of the first-order sidebands (same parameters as in Fig. 8.3).

given by the energy spacing ΔE between the resonances. The envelope of the decaying beat signal is given by an exponential factor $\exp\left(-(\Gamma_1 + \Gamma_2)\, t/2\right)$ and thus depends on the arithmetic mean of the inverse lifetimes. Finally, the underlying constant background is due to the fast direct (non-resonant) ionization.

Fig. 8.6 shows the pump-probe spectra for the same parameters as in Fig. 8.5, however, for the case of two Lorentz resonances ($q_k \to \infty$). The characteristic beating signal in the sidebands, similar to the one in Fig. 8.5 is clearly visible.

In order to illustrate the dependence on the phases of the resonant amplitudes, we present in Fig. 8.7 the intensities, integrated over the width of the sideband, for a relative phase 0 (Fig. 8.7a) or π (Fig. 8.7b) between the resonant amplitudes a_k. The beat pattern is noticeably different, in particular the phase of the beat signal is shifted by approximately π. This observation

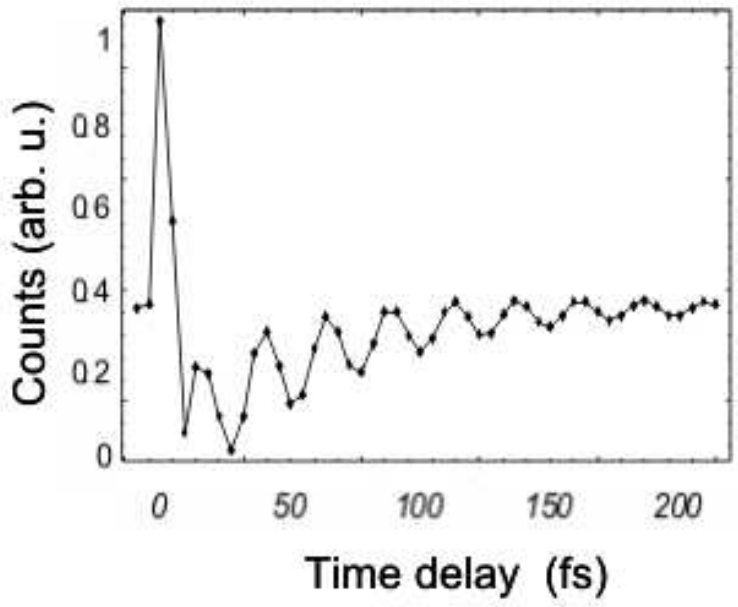

Figure 8.5: First-order sideband intensity at $E = (E_a + E_b)/2 + \omega_L$ as a function of pump-probe delay for two window resonances with parameters: $E_a = 76.32$ eV and $E_b = 76.46$ eV with the widths $\Gamma_a = 25.2$ meV and $\Gamma_b = 14.2$ meV corresponding to lifetimes of about $27fs$ and $47fs$, respectively.

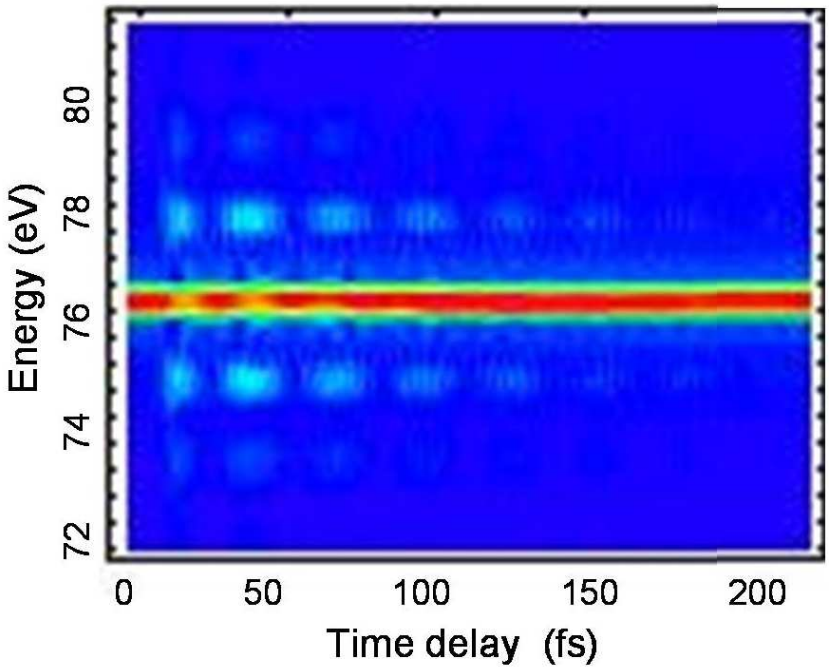

Figure 8.6: Pump-probe spectra for the same parameters as Fig. 8.5, however Lorentz resonances ($q_k \to \infty$) instead of window resonances. The sidebands show the characteristic beating signal.

indicates that information on the excitation amplitudes can be extracted from streaking images.

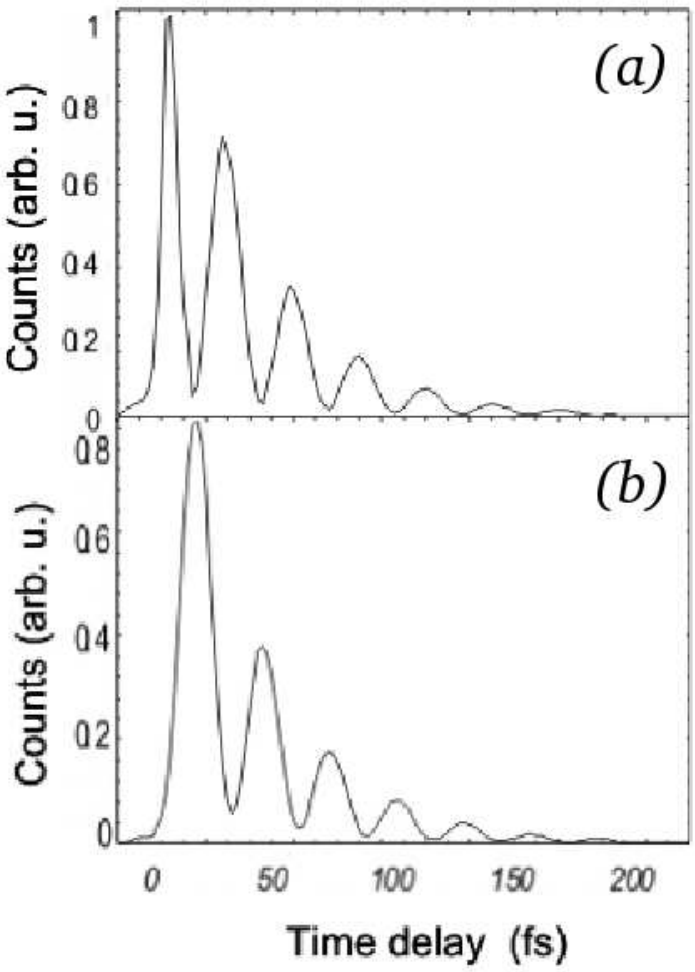

Figure 8.7: First order sideband population integrated over the width of the sideband. Same parameters as Fig. 8.6. (a) Relative phase between amplitudes a_k: $\phi = 0$; (b) $\phi = \pi$.

Under the simplifying assumption of a cw-laser as probe pulse, the ionization probability at the energy of the first order sideband can be written as

$$P = \frac{1}{4}|J_1\left(\frac{p_z EL}{\omega^2}\right)\int_{-\infty}^{\infty}\left(V_a\langle a|d|g\rangle\tilde{f}_a + V_b\langle b|d|g\rangle\tilde{f}_b\right)dt|^2. \tag{8.12}$$

J_1 is the Bessel function of order 1 and $\tilde{f}_k$ is the convolution of a Gaussian and an exponentially decaying function,

$$\tilde{f}_k(t) = \int_{-\infty}^{t} dt' f_X(t') e^{(-\Gamma_k/2 \pm i\Delta E/2)(t-t')} \tag{8.13}$$

For the amplitude corresponding to the resonance $|a\rangle$ a plus has to be used in the exponent in the integral, and a minus is used for the resonance $|b\rangle$. The plus and minus signs result from the symmetry of the problem. The energy of the resonant state a is $\Delta E/2$ below the excitation energy $E_g + \omega_x$, and the energy of the resonant state b is $\Delta E/2$ above the excitation energy. Eq. (8.12) can be derived by evaluating Eq. (8.7) at the energy of the first order sideband $E_r + \omega_L$. We expand the exponential term with the Volkov phase in a series of Bessel functions. Since the first order sideband originates from the absorption of one photon, only the first term in the sum of Bessel functions, which is proportional to $J_1\left(\frac{p_z E_L}{\omega^2}\right)$, contributes. From equation (8.12) the time-differential ionization probability at the energy $E_r + \omega_L$ can be easily extracted:

$$\frac{dP}{dt} \propto |\left(V_a\langle a|d|g\rangle\tilde{f}_a + V_b\langle b|d|g\rangle\tilde{f}_b\right)|^2 \tag{8.14}$$

Fig. 8.8 shows the time-differential ionization probability for the same parameters as in Fig. 8.7 except that the probe pulse is a cw-laser. From the remarkable agreement of Fig. 8.8 with Fig. 8.7 we can conclude that non-trivial information about the ionization process happening on a femtosecond time scale can be extracted directly from the pump-probe spectra.

In this chapter we have presented attosecond streaking images of Fano resonances including coherent excitation of nearby resonances. We could show that these spectra contain information that is only partially accessible by other, time-integral spectroscopic techniques. We have discussed that near-degenerate resonances with significantly different lifetimes can be resolved through their different appearance in the streaking image. Moreover, off-diagonal elements of the excitation density matrix influence the streaking image and are thus accessible.

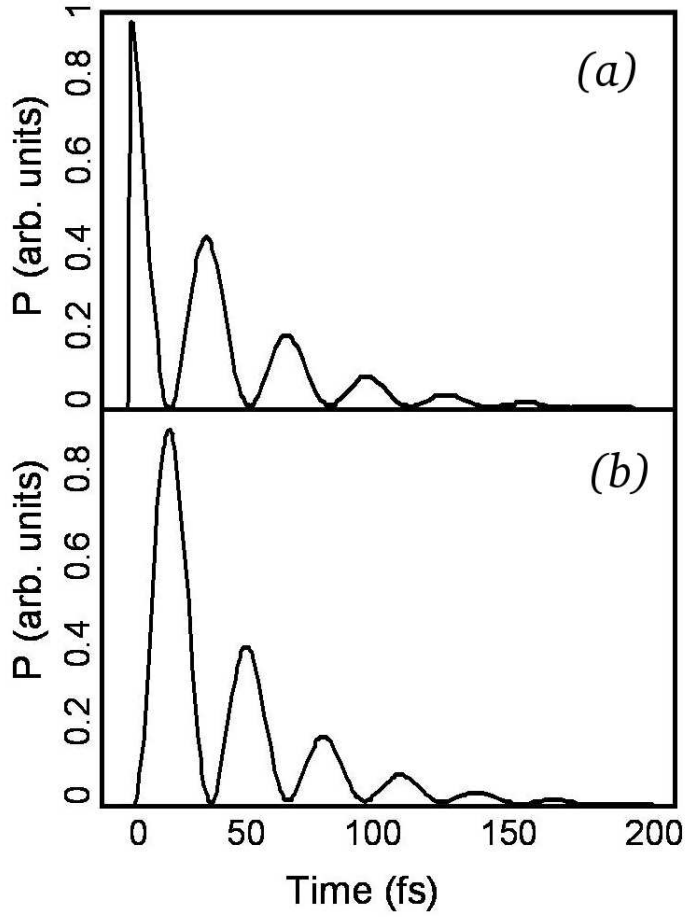

Figure 8.8: Time-differential ionization probability. (a) Relative phase between the amplitudes: $\phi = 0$; (b) $\phi = \pi$.

Chapter 9

Conclusions and Summary

Motivated by the rapid progress in laser technology, we have investigated in this thesis the ionization dynamics of atoms in femto- and attosecond laser pulses. We have especially focused on the few-cycle aspects of the pulses in the ionization process. In contrast to longer pulses, it is not possible to specify a certain wavelength or intensity for a few-cycle pulse. The intensity changes with each cycle, so that within a few cycles the field strength rises from zero to its maximum value and the width in the frequency domain of the few-cycle pulse is inversely proportional to the pulse length. These aspects of ionization in a short pulse are analyzed in chapters three and four for the case of above-threshold ionization, where we have focused on the for experiment important case of argon. The main feature of above-threshold ionization (ATI) spectra are ATI peaks separated by the photon energy. The position of an ATI peak is determined by the photon energy, the number of the absorbed photons and the ionization potential. However, the energy position of the levels shift in the field. This shift is near the threshold equal to the ponderomotive potential. Thus the effective ionization potential, given by the sum of the ionization potential of the atom and the ponderomotive potential, depends quadratically on the laser field. We analyze in chapter three this shifting ponderomotive potential, which leads to subpeaks within an ATI peak in the energy spectrum (Wickenhauser et al. [14], Bardsley et al. [19]). These peaks are sensitive to the pulse duration and the pulse envelope and are a general feature of ionization spectra originating from a short, intense laser pulse. The finite width of the pulse in the frequency domain manifests itself in the width of the ATI peaks and the missing of isolated

Freeman resonances in the spectrum, as would be observed with a longer pulse having a well defined frequency.

At first sight, the interplay of atomic and laser forces seems to cause a rather complex behavior in the ionization process. Fortunately, for many problems in atto- and femtosecond physics, one can separate the dynamics into a domain 'inside' the atom, where atomic forces dominate, and 'outside', where the laser force dominates. Therefore a main part of this thesis is dedicated to the investigation of the accuracy of the so called 'strong field approximation (SFA)' model, which is one of the most popular models used in the field of laser-atom interaction. The SFA model is based on two main approximations. First, the influence of the core potential on the ionized electrons is neglected and second, all intermediate bound states except the ground state are neglected. In chapters three and four we compare the results of the SFA model with the ab initio solution of the TDSE for the energy spectra and the angle-resolved momentum distributions for several laser parameters. This comparison is on the one hand important to understand for which problems the SFA model provides reliable results. On the other hand the comparison itself is a powerful tool to analyze the results obtained with the numerical solution of the TDSE.
In our study we found that many aspects of the low-energy spectra as well as of the angle-resolved momentum spectra can be explained with the simple SFA model. Discrepancies between the two calculations are caused by the action of the core potential on the ionized electrons or/and the effect of intermediate bound states in the ionization process.

The in chapter four performed study on angle-resolved electron momentum spectra was motivated by recent experiments (Rudenko et al. [20], Maharjan et al. [21]). We have investigated the dominant structures in the momentum spectra. The angle-resolved spectra give information about the position, parity and dominant angular momentum of the ATI peaks. We observe that the laser-induced subpeaks within one ATI peak all have the same parity. Thus, by the parity it is straightforward to distinguish the subpeaks belonging to one ATI peak from the next ones in the angle-resolved momentum spectra. Additionally, in this chapter we have addressed the question whether a dip or a peak is observed in the projection on the momentum

parallel to the polarization direction. In recent experiments (Rudenko et al. [20], Moshammer et al. [58, 94]) it was found that the spectra for helium and neon show a pronounced dip in the parallel-momentum distribution, while for argon a peak was observed. Since this dip has a striking similarity to the momentum-spectra observed for non-sequential double ionization the first interpretation of this dip was rescattering of the ionized electron. In a subsequent study the influence of the Coulomb potential on the ionized electron was investigated in a semiclassical model (Dimitriou et al. [61]) and it was shown that the Coulomb potential leads to a similar structure in the parallel momentum distribution. In (Arbo et al. [59]) structures in the momentum spectra were attributed to a Ramsauer-Townsend Diffraction pattern. In a recent improved experiment (Rudenko et al. [20]) it was however shown that not only a dip is observed in the momentum spectra but also a series of sharp structures which positions do not change with the intensity. This latter observation leads to the conclusion that Freeman resonances are most probably responsible for the observed structures in the angle-resolved momentum spectra in experiment. However, recent measurements for argon (Maharjan et al. [21]) which showed a deep dip for 400 nm questioned the origin of this dip again. In this thesis we could give an alternative explanation for the observed dip. We prove the influence of the parity of the low-energy electrons on the observed structures in the momentum spectra. Our calculations agree well with experiment for argon and neon for 400 nm which proves the reliability of the theoretical as well as the experimental results. Additionally, our detailed study covering a wide range of laser parameters helped to solve the confusion caused by the various explanations of the dip in literature.

In the following chapters we discuss the ionization dynamics with an attosecond pulse in the presence of a femtosecond, probe laser pulse. Pump-probe experiments are the most direct approach to tracing fast dynamics in the time domain. The extension of time-resolved (pump-probe) spectroscopy to ultrafast electronic processes taking place deep inside atoms has so far been frustrated by simultaneous requirements of short wavelengths (i.e. high photon energy) and sub-femtosecond pulse duration. Additionally, for a straightforward interpretation of spectroscopic data, isolated pulses were needed. With single attosecond pulses and a precisely timed laser pulse at hand, the streak-camera concept (Drescher et al. [11]) could be extended

to study the ionization dynamics of core electrons. In a recent experiment on a krypton gas target the lifetime of an Auger transition was measured to be 8 femtoseconds. The attosecond pulse excites a core electron and the probe laser pulse is used to obtain information about the ionization process. Two limiting regimes can be distinguished. For short lifetimes of the resonant state the resulting spectrum shifts periodically up and down, following the oscillation of the probe laser field. In the limit of long lifetimes of the resonance, the pulse envelope samples the ionization process. We have investigated in this thesis the more complex behavior of the excitation of a Fano resonance. We found that in the pump-probe spectra it is possible to separate the two ionization channels for an autoionizing decay, the resonant and the direct ionization channel. E.g. in the case of a long lifetime of the resonance, the resonant channel leads to sidebands in the spectrum while the direct channel is responsible for the up and down shifted part of the spectra. We have generalized our description to the case of two (overlapping) resonances. We find that in the case of the coherent excitation of two Fano resonances a beating in the signal of ionized electrons can be seen, where the beating frequency is proportional to the energy spacing between the two resonances. We show that this beating signal is sensitive to the relative sign of the excitation matrix elements for the two resonances. Thus information about the off-diagonal elements of the density matrix can be obtained. In the last figure of this thesis we show that the time-differential ionization probability for the two resonances is almost identical to the signal seen in the pump-probe spectra. This clearly proves that non trivial information about the ionization process happening on a femtosecond time scale can be directly extracted from the pump-probe spectra.

Bibliography

[1] G. Steinmeyer, D. H. sutter, L. Gallmann, N. Matuschek, and U. Keller, Science **286**, 1507 (1999).

[2] A. Baltuska, Z. Wei, M. S. Pshenichnikov, D. A. Wiersma, and R. Szipocs, Appl. Phys. B **65**, 175 (1997).

[3] M. Nisoli, S. S. ans S. De, O. Svelto, S. Sartania, Z. Cheng, M. Lenzner, C. Spielmann, and F. Krausz, Appl. Phys. B **65**, 189 (1997).

[4] U. Morgner, F. Kartner, S. Cho, Y. Chen, H. A. Haus, J. Fujimoto, E.P.Ippen, V. Scheuer, G. Angelow, and T.Tschudi, Opt. Letter **24**, 631 (1999).

[5] D. Sutter, G. Steinmeyer, L. Gallmann, N. Matuschek, F. Morier-Genoud, U. Keller, G. Angelow, and T. Tschudi, Opt. Letter **24**, 631 (1999).

[6] A. Shirakawa, I. Sakane, M. Takasaka, and T. Kobayashi, Appl. Phys. Lett. **74**, 2268 (1999).

[7] T. Brabec and F. Krausz, Rew. Mod. Phys. **72**, 545 (2000).

[8] V. Keldysh, JETP **20**, 1307 (1965).

[9] M. Hentschel, R. Kienberger, C. Spielmann, G. A. Reider, N. Milosevic, T. Brabec, P. B. C. U. Heinzmann, M. Drescher, and F. Krausz, Nature **414**, 509 (2001).

[10] E. Goulielmakis, M. Uiberacker, R. Kienberger, A. Baltuska, V. Yakovlev, A. Scrinzi, T. Westerwalbesloh, U. Kleineberg, U. Heinzmann, M. Drescher, et al., Science **305**, 1267 (2004).

[11] M. Drescher, M. Hentschel, R. Kienberger, M. Uiberacker, V. Yakovlev, A. Scrinzi, T. Westerwalbesloh, U. Kleineberg, U. Heinzmann, and F. Krausz, Nature **419**, 803 (2002).

[12] O. Smirnova, V. Yakovlev, and A. Scrinzi, Phys. Rev. Lett. **91**, 253001 (2003).

[13] M. Lewenstein, P. Balcou, M. Y. Ivanov, A. L'Huillier, and P. B. Corkum, Phys. Rev. A **49**, 2117 (1994).

[14] M. Wickenhauser, X. M. Tong, and C. D. Lin, Phys. Rev. A **73**, R011401 (2006).

[15] M. Wickenhauser, X. M. Tong, D. G. Arbó, J. Burgdörfer, and C. D. Lin, submitted to PRL (2006).

[16] X. M. Tong and S.-I. Chu, Chem. Phys. **217**, 119 (1997).

[17] X. M. Tong and S.-I. Chu, Phys. Rev. A **61**, 031401(R) (2000).

[18] R. Wiehle, B. Witzel, H. Helm, and E. Cormier, Phys. Rev. A **67**, 063405 (2003).

[19] J. N. Bardsley, A. Szöke, and M. J. Comella, J. Phys. B **21**, 3899 (1988).

[20] A. Rudenko, K. Zrost, C. D. Schröter, V. L. B. de Jesus, B. Feuerstein, R. Moshammer, and J. Ullrich, J. Phys. B **37**, L407 (2004).

[21] C. M. Maharjan, A. S. Alnaser, I. Litvinyuk, P. Ranitovic, and C. L. Cocke, J. Phys. B **39**, 1955 (2006).

[22] U. Fano, Phys. Rev. **124**, 1866 (1961).

[23] U. Fano, Nuovo Cimento **12**, 154 (1935).

[24] P. Lambropoulos and P. Zoller, Phys. Rev. A **24**, 1 (1981).

[25] M. Wickenhauser, J. Burgdoerfer, F. Krausz, and M. Drescher, Phys. Rev. Lett. **94**, 023002 (2005).

[26] Z. X. Zhao and C. D. Lin, Phys. Rev. A **71**, 060702(R) (2005).

[27] R. R. Jones, Phys. Rev. Lett. **76**, 3927 (1996), URL `http://link.aps.org/abstract/PRL/v76/p3927`.

[28] C. O. Reinhold, J. Burgdörfer, M. T. Frey, and F. B. Dunning, Phys. Rev. A **54**, R33 (1996), URL `http://link.aps.org/abstract/PRA/v54/pR33`.

[29] J. Ahn, T. C. Weinacht, and P. H. Bucksbaum, Science **287**, 463 (2000).

[30] M. Wickenhauser, J. Burgdorfer, F. Krausz, and M. Drescher, J. of modern optics **53**, 247 (2006).

[31] H. Friedrich, *Theoretical Atomic Physics* (Springer Verlag) (1998).

[32] J. C. Diels and W. Rudolph, *Ultrashort Laser Pulse Phenomena* (Academic Press) (1995).

[33] J. Jackson, *Classical Electrodynamics* (John Wiley & Sons Inc., New York, 1999).

[34] L. F. DiMauro and P. Agostini, *Advances in Atomic, Molecular and Optical Physics* (Academic Press, New York), Vol. 35, (1995).

[35] P. Agostini, F. Fabre, G. Mainfray, G. Petite, and N. K. Rahman, Phys. Rev. Lett. **42**, 1127 (1979).

[36] E. Mevel, P. Breger, R. Trainham, G. Petite, P. A. nad A. Migus, J. Chambaret, and A. Antonetti, Phys. Rev. Lett **70**, 406 (1993).

[37] L. F. DiMauro and P. Agostini, Adv. At. Mol. Opt. Phys. **35**, 79 (1995).

[38] M. V. Ammosov, N. B. Delone, and V. P. Krainov, JETP **64**, 1191 (1986).

[39] C. Z. Bisgaard and L. B. Madsen, Am. J. Phys. **72**, 249 (2004).

[40] A. M. Perelomov, V. S. Popov, and M. V. Terentev, JETP **23**, 924 (1966).

[41] N. B. Delone and V. P. Krainov, J. Opt. Soc. Am. B **8**, 1207 (1991).

[42] F. H. M. Faisal, J. Phys. B **6**, L89 (1973).

[43] H. R. Reiss, Phys. Rev. A **22**, 1786 (1980).

[44] D. Bauer, D. B. Milosevic, and W. Becker, Phys. Rev. A **72**, 023415 (2005).

[45] D. Bauer, D. B. Milosevic, and W. Becker, quant-ph/0504053 (2005).

[46] J. Wang, , S. Chu, and C. Laughlin, Phys. Rev. A **50**, 3208 (1994).

[47] D. Telnov and S. Chu, Phys. Rev. A **59**, 2864 (1999).

[48] M. J. Nandor, M. A. Walker, L. D. VanWoerkom, and H. G. Muller, Phys. Rev. A **60**, R1771 (1999).

[49] E. Cormier, D. Garzella, P. Geger, P. Agostini, G. Cheriaux, and C. Leblanc, J. Phys. B **34**, L9 (2001).

[50] A. Assion, T. Baumert, J. Helbing, V. Seyfried, and G. Gerber, Phys. Rev. A **55**, 1899 (1997).

[51] G. G. Paulus, W. Nicklich, F. Zacher, P. Lambropoulos, and H. Walther, J. Phys. B **29**, L249 (1995).

[52] R. R. Freeman, P. H. Bucksbaum, H. Milchberg, S. Darack, D. Schumacher, and M. E. Geusic, Phys. Rev. Lett. **59**, 1092 (1987).

[53] V. D. Rodriguez, E. Cormier, and R. Gayet, Phys. Rev. A **69**, 053402 (2004).

[54] F. Lindner, M. G. Schatzel, H. Walther, A. Baltuška, E. Goulielmakis, F. Krausz, D. B. Milošević, D. Bauer, W. Becker, and G. G. Paulus, Phys. Rev. Lett. **95**, 040401 (2005).

[55] X. M. Tong and C. D. Lin, J. Phys. B **38**, 2593 (2005).

[56] G. D. Gillen and L. D. VanWoerkom, Phys. Rev. A **68**, 033401 (2003).

[57] C. C. Chirilă and R. M. Potvliege, Phys. Rev. A **71**, 021402(R) (2005).

[58] R. Moshammer, J. Ullrich, B. Feuerstein, D. Fischer, A. Dorn, C. D. Schröter, J. R. C. Lopez-Urrutia, C. Hoehr, H. Rottke, C. Trump, et al., Phys. Rev. Lett. **91**, 113002 (2003).

[59] D. G. Arbo, S. Yoshida, E. Persson, K. I. Dimitriou, and J. Burgdörfer, Phys. Rev. Lett. **96**, 143003 (2006).

[60] J. Chen and C. H. Nam, Phys. Rev. A **66**, 053415 (2002).

[61] K. I. Dimitriou, D. G. Arbó, S. Yoshida, E. Persson, and J. Burgdörfer, Phys. Rev. A **70**, 061401(R) (2004).

[62] F. H. Faisal and G. Schlegel, J. Phys. B **38**, L223 (2005).

[63] V. P. Krainov and B. Shokri, JETP **80**, 657 (1999).

[64] G. S. Agarwal, S. L. Haan, K. Burnett, and J. Copper, Phys. Rev. A **26**, 2277 (1982).

[65] J. Zakrzewski, J. Phys. B **17**, 719 (1984).

[66] L. Armstrong, E. Constatine, E. Theodosiou, and M. J. Wall, Phys. Rev. A **18**, 2538 (1978).

[67] G. Alber and P. Zoller, Phys. Rev. A **29**, 2290 (1984).

[68] Z. X. Zhao and C. D. Lin, Phys. Rev. A **71**, 060702(R) (2005).

[69] M. V. Fedorov, *Atomic and Free Electrons in a Strong Light Field* (World Sci.,Singapore) (1997).

[70] J. Faist, F. Capasso, C. Sirtori, K. W. West, and L. N. Pfeiffer, Nature **390**, 589 (1997).

[71] V. Madhaven, W. Chen, T. Jamneala, M. F. Crommie, and N. S. Wingreen, Science **280**, 567 (1998).

[72] J. Göres, D. Goldhaber-Gordon, S. Heemeyer, M. A. Kastner, H. Shtrikman, D. Mahalu, and U. Meirav, Phys. Rev. B **62**, 2188 (2000).

[73] J. Burgdorfer and R. Morgenstern, Phys. Rev. A **38**, 5520 (1988).

[74] J. Itatani, F. Quere, G. L. Yudin, M. Y. Ivanov, F. Krausz, and P. B. Corkum, Phys. Rev. Lett. **88**, 173903 (2002).

[75] R. K. et al., Nature **427**, 817 (2004).

[76] C. Dzionk, W. Fiedler, M. v. Lucke, and P. Zimmermann, Phys. Rev. Lett. **62**, 878 (1988).

[77] U. Eichmann, T. Gallagher, and R. M. Konig, Phys. Rev. Lett. **90**, 233004 (2003).

[78] M. Dantus, R. M. Bowman, and A. H. Zewail, Nature **343**, 737 (1990).

[79] M. Hase, K. Mizoguchi, H. Harima, S. Nakashima, and K. Sakai, Phys. Rev. B **58**, 5448 (1998).

[80] J. A. Yeazell and J. C. R. Stroud, Phys. Rev. Lett. **60**, 1494 (1988).

[81] C. Raman, C. W. S. Conover, C. I. Sukenik, and P. H. Bucksbaum, Phys. Rev. Lett. **76**, 2436 (1996).

[82] C. A. Nicolaides, T. Mercouris, and Y. Komninos, J. Phys. B **35**, L271 (2002).

[83] T. Mercouris, Y. Komninos, and C. A. Nicolaides, Phys. Rev. A **69**, 032502 (pages 9) (2004).

[84] R. Kienberger, E. Goulielmakis, M. Uiberacker, A. Baltuska, V. Yakovlev, F. Bammer, A. Scrinzi, T. Westerwalbesloh, U. Kleineberg, U. Heinzmann, et al., Nature **427**, 817 (2004).

[85] K. Kobayashi, H. Aikawa, S. Katsumoto, and Y. Iye, Phys. Rev. B **68**, 235304 (pages 8) (2003).

[86] K. Kobayashi, H. Aikawa, S. Katsumoto, and Y. Iye, Phys. Rev. Lett. **88**, 256806 (2002).

[87] A. A. Clerk, X. Waintal, and P. W. Brouwer, Phys. Rev. Lett. **86**, 4636 (2001).

[88] P. von den Straten and R. Morgenstern, Comments At. Mol. Phys. **19**, 243 (1986).

[89] A. Magunov and S. Strakhova, Phys. Rev. B **68**, 245305 (2003).

[90] P. E. Coleman and P. L. Knight, J. Phys. B **15**, L235 (1982).

[91] P. E. Coleman, P. L. Knight, and K. Burnett, Opt. Commun. **42**, 171 (1982).

[92] X. Yang, J. Burgdorfer, and J. Muller, Chaos, Solitons and Fractals **5**, 1235 (1995).

[93] M. Domke, K. Schulz, G. Remmers, G. Kaindl, and D. Wintgen, Phys. Rev. A **53**, 1424 (1996).

[94] R. Moshammer, B. Feuerstein, W. Schmitt, A. Dorn, C. D. Schröter, J. Ullrich, H. Rottke, C. Trump, M. Wittmann, G. Korn, et al., Phys. Rev. Lett. **84**, 447 (2000).